Implications of a highly convective lunar magma ocean: Insights from phase equilibria modeling

K.A. Cone[a,b], S.M. Elardo[c], F.J. Spera[d], W.A. Bohrson[a], R.M. Palin[e]

[a]Department of Geology and Geological Engineering, Colorado School of Mines, CO, USA
[b]Department of Earth and Environmental Sciences, University of Rochester, NY, USA
[c]Department of Geological Sciences, University of Florida, FL, USA [d]Department of Earth Science and Earth Research Institute, University of California, Santa Barbara, USA [e]Department of Earth Sciences, University of Oxford, UK

*Corresponding author and current address: Kim A. Cone (kimacone@gmail.com), Department of Earth and Environmental Sciences, University of Rochester, Rochester, NY, USA

Abstract

The Moon's internal structure was largely defined within the first 200 million years following the initial Moon-forming impact. During this period, the molten Moon (a lunar magma ocean, or LMO) lost most of its heat through early vigorous convection, crystallizing and forming an initial cumulate stratigraphy through robust equilibrium crystallization followed by fractional crystallization once the LMO became sufficiently viscous. This rheological transition is estimated to have occurred at 50% to 60% LMO solidification, and although the petrological effects of the regime switch have been frequently investigated at the lower value, such effects at the upper limit have not been formally examined until now. Given this scenario, we present two new internally consistent, high-resolution models that simulate the solidification of a deep LMO of Earth-like bulk silicate composition at both rheological transition values, focusing on the petrological characteristics of the evolving mantle and crust. The results suggest that increasing the volume of early suspended solids from the oft-examined 50% to 60% may lead to non-trivial differences. The appearance of mantle garnet in absence of a refractory-element enriched bulk silicate Moon composition, a bulk mantle richer in orthopyroxene than olivine, a lower density upper mantle, and a thinner crust, are all characteristics resulting from a volumetric increase in equilibrium crystallization solids. In addition, we find that the low density of late-stage, silica-enriched melts may prevent plagioclase from floating, interfering with the long-term building of a plagioclase flotation crust. As the ability of a lunar magma ocean to suspend crystals is directly tied to the Moon's early thermal state, the degree of early LMO convection – and the early solar system environment that drives it – require as much consideration in petrological LMO models as more well-investigated parameters such as bulk silicate Moon composition and initial magma ocean depth.

Keywords

Moon, lunar magma ocean, lunar petrology, lunar evolution, lunar crust

1. Introduction

One of the most profound consequences of the high-energy, Moon-forming giant impact was the molten state the Moon assumed immediately afterward (e.g. Canup and Asphaug, 2001; Canup, 2004; Cuk and Stewart, 2012; Lock et al., 2018, 2020), commonly referred to as the lunar magma ocean (LMO). Subsequent cooling of the LMO over tens (Elkins-Tanton et al., 2011) to possibly hundreds of millions of years (Maurice et al., 2020) led to density-driven separation of minerals from melt and eventually, a differentiated solid Moon. LMO cooling models, at least from a petrological and compositional standpoint, have largely focused on the effects of various bulk silicate Moon compositions (BSMCs) and/or LMO depths on whole-Moon structure. These two parameters (along with others) are typically examined within either one of two end-member crystallization regimes: 1) a two-stage process of equilibrium crystallization (e.g. Tonks and Melosh, 1990; Elardo et al., 2011) followed by fractional crystallization, or 2) a fully fractional crystallization model (e.g. Rapp and Draper, 2018; Schwinger and Breuer, 2022).

More than ~40 BSMCs have been considered in the literature (Cone et al., 2020; 2021 and references therein), although two serve as frequently explored end-member compositions: the refractory element-enriched Taylor Whole Moon (TWM; Taylor, 1982) and the Earth-like Lunar Primitive Upper Mantle (LPUM; Longhi, 2006). Models using the TWM composition produce garnet as the dominant Al-bearing phase at high pressure when coupled with an LMO greater than 1000 km deep (e.g. Elardo et al., 2011; Jing et al., 2022; Kraettli et al., 2022; Schmidt et al., 2022), as the TWM composition is enriched in Al and Ca by 50% relative to bulk silicate Earth. Shallower LMO models do not generate garnet, as the base of the LMO does not reach the necessary pressure for its stabilization (e.g. Charlier et al., 2018). Models using the LPUM composition have not produced garnet in the deep mantle before the crystallization front moves to lower pressure, instead producing a lower mantle dominated by olivine and some orthopyroxene (e.g. Elardo et al., 2011; Johnson et al., 2021). The results of the Gravity Recovery and Interior Laboratory (GRAIL) mission, however, have made refractory element-enriched compositions such as the TWM untenable. The TWM composition was developed in order to explain an inferred crustal thickness of ~73 km produced from a shallow (e.g. ~500 km) LMO, which would require the LMO to be enriched in refractory elements. Crustal thickness estimates from the GRAIL mission now estimate the feldspathic crust to be ~34–43 km thick (e.g., Wieczorek et al., 2013) and modern giant impact models predict deep to whole Moon melting, thus obviating the need for refractory element enrichment. More recently, even LMO models using Earth-like compositions and a deep LMO produce crustal thicknesses exceeding GRAIL estimates unless an altered thermal state is invoked (e.g. Charlier et al., 2018; Elardo et al., 2020). Some models also produce a quartz-rich layer at the end stages of LMO solidification, which can increase crustal thickness while lowering its density, although direct evidence for widespread quartz/silica crystallization from the LMO is lacking.

The two-stage model reflects an initially robust convective regime that forces early equilibrium crystallization. Once the LMO is sufficiently crystal rich, a regime switch to fractional crystallization occurs. This rheological transition is estimated to occur at ~50 vol.% LMO solids (Tonks and Melosh, 1990; Snyder et al., 1992; Spera, 1992). However, this crystal lockup point can occur at $\geq$ 60 vol.% solids (e.g. Abe, 1995; Solomatov, 2007; Costa et al., 2009) if convection is vigorous, the effects of which have not been previously been modeled for the cooling of a deep LMO of LPUM composition.

The first goal of this study was to create two LMO models that simulate the solidification of a full-depth (~1400 km) LMO using an Earth-like BSM composition (LPUM) and a two-stage crystallization regime with rheological transitions at both 50% and 60% LMO volume solids. Both models are created using the same internally-consistent thermodynamic database and solidification protocol to allow direct comparison. Although BSMCs are frequently varied (holding other variables constant) in LMO models to assess the effects on whole-Moon petrological structure, the effects from varying the duration of early convection while holding the BSMC constant has not been previously explored in depth.

The second goal of this study was to compare the results and approaches of our LPUM LMO solidification models against other works for any significant differences in inferred whole-Moon petrological structure. We characterized geochemical, petrological, and physical aspects of the modeled crusts, mantles, and crust-mantle transition zones assuming that a mantle overturn did not occur until after near-complete solidification (e.g. Boukaré et al., 2017). The results of this comparison constrain the differences in structure and composition of two primitive, differentiated lunar interiors that crystallize under two plausible durations of an early turbulent convective LMO.

2. The LMO Model: Starting Parameters and Process Flow

2.1. A Bulk Silicate Moon Composition for a Deep LMO

~~The TWM composition continues to be explored in recent LMO cooling models and was initially derived based on an assumption of a 73-km thick alumina-rich crust. This composition no longer serves as a compelling choice for modeling since the GRAIL-era finding for a 34-43-km thick crust.~~ The LPUM composition used here (Longhi, 2006) reflects a primitive terrestrial upper mantle (as a modification of Hart and Zindler, 1986) and is similar to bulk silicate Earth. In addition, giant impact work suggesting extreme source homogenization of the co-evolving Earth-Moon system (e.g. Lock et al., 2018; 2020) and evidence for an Earth-like Moon-forming impactor (Dauphas et al., 2014) support the use of BSMCs that are similar to bulk silicate Earth. ~~For example, Hauri et al. (2015) proposed a volatile-reduced version of the McDonough and Sun (1995) bulk silicate Earth.~~

2.2. Pressure-depth relationship

We assumed a small lunar core based on the seismic interpretations in Weber et al. (2011) and on those summarized in Garcia et al. (2019). Assuming a lunar radius of 1737.15 km (Williams et al., 2014), the core radius was set to 330 km (Weber et al., 2011), leaving an ~1400-km thick magma ocean (D_{LMO} = ~1400 km). LMO depth was converted to pressure (P) assuming unform spherical density (Turcotte and Schubert, 2002),

$$P = 2/3\ \pi\ \rho_{MP}^2\ G(R_{FULL}^2 - r^2) \qquad \textbf{(Eq. 1)}$$

where the mean primitive lunar density ρ_{MP} = 3345.56 kg m^{-3} (Williams et al., 2014), the universal gravitational constant G = 6.674 x 10^{-11} m^3 kg^{-1} s^{-2}, R_{FULL} = 1737.15 km, and r is the LMO radius that varies with depth. This method of approximating changes in P with depth (z)

does not consider density evolution during LMO solidification, although still provides a reasonable means for estimating a *P*-*z* profile and has been previously employed in LMO models (e.g. Elkins-Tanton et al., 2011; Fig. S1 in Supporting Information).

2.3. Phase equilibria characteristics

All phase equilibria were calculated using the Gibbs free energy minimizer Perple_X (version 6.9.0; Connolly, 2005; 2009), an internally consistent thermodynamic dataset (hp633ver.dat; Holland and Powell, 2011; Holland et al., 2018), and relevant solid solution models (Jennings and Holland,15; Green et al., 2016; Holland et al., 2018; White et al., 2000; 2014) over the *P*–*T* conditions relevant to LMO depths. Melt and solid phases (olivine (OL), orthopyroxene (OPX), garnet (GT), spinel (SP), clinopyroxene (CPX), plagioclase (PL), ilmenite (ILM), quartz (QTZ), and a potassic feldspar sanidine (SAN)) were considered in the anhydrous nine-component SiO_2-MgO-FeO-Al_2O_3-CaO-Cr_2O_3-TiO_2-Na_2O-K_2O system, listed here in order of decreasing wt.% oxide. Perple_X utilizes a gridded minimization approach where phase boundaries are continuously refined according to user-defined resolution settings (cf. Connolly, 2005; 2009). A summary of the solid solution models and grid resolution settings are included in Supporting Information (Fig. S2). Phase boundary uncertainties within a single phase-diagram are estimated at ±1 kbar and ± 50°C at the 2σ level (Powell and Holland, 2008; Palin et al., 2016). FeO was the only form of iron oxide considered for a silicate LMO at or below an IW buffer (Sato et al., 1973; Papike et al., 2015). The geikielite endmember of the ilmenite solid solution model was excluded in our calculations due to reports that it becomes overstabilized at high temperature conditions (Green et al., 2016).

2.4. Pressure-temperature conditions for crystallization

The lunar mantle is assumed to have solidified from the 'bottom-up' as crystallization proceeds (e.g. Solomatov, 2000; Elkins-Tanton, 2012) and *P*-*T* values were approximated using linear adiabats calculated for each cooling step. The LMO was treated as a quasi-isothermal system wherein large-scale vigorous convection produces a well-stirred LMO, thereby efficiently distributing heat from top to bottom. As adiabatic slopes for an initially hot, small silicate body like the Moon are expected to be steep (e.g. Tonks and Melosh, 1990), the temperature difference between the LMO surface and base would be insignificant over the 1400-km LMO depth. The adiabatic change in temperature with pressure was approximated by

$$\frac{dT}{dP} = V\,T_{BASE}\,C_p^{-1} \qquad \textbf{(Eq. 2)}$$

where α is the coefficient of thermal expansion, V is specific volume, T_{BASE} is the base temperature of a well-stirred LMO, and Cp is the LMO heat capacity. Values for these parameters were determined by Perple_X.

2.5. Process flow: Convection and crystallization regimes

We modeled the effects of a solidifying full-depth LMO after core formation using the two-stage model. Stage one reflected a magma ocean that vigorously convects until 50% or 60% solids (referred to as the EQX50 and EQX60 models, respectively) are achieved, after which stage two simulated fractional crystallization until the LMO is fully solid (referred to as the EQX50 and EQX60 models, respectively). We chose a two-stage model over a fully fractional model due to initial constraining assumptions that suggest an early turbulent regime (Solomatov, 2007; Spera, 1992; Tonks and Melosh, 1990): 1) the LMO begins as a low viscosity, ultramafic melt; 2) the Moon is a small body with low gravitational acceleration (1.6 m s^{-2} at the surface) and so is conducive to extended crystal suspension; and 3) heat loss is efficient due to the temperature contrast between the LMO base (~2200 K) and the free surface where the temperature of space is ~240 K. All of these factors promote turbulence.

The 60 vol.% rheological lockup value represents an estimate of maximum crystal loading for early vigorous convection. A quantitative scaling analysis is here expressed as a dimensionless number, *R*, that compares crystal settling velocity against vertical convective velocity:

$$R = \frac{\Delta\rho g\, d^2\, L}{18\,\kappa\,\eta_{melt}}\, Ra^{-3/7}(1-\theta)^m \text{¿¿} \qquad \textbf{(Eq. 3)}$$

where $\Delta\rho$ is the mean crystal-melt density difference, g is gravitational acceleration, d is the mean crystal diameter, L is the LMO depth, κ is thermal diffusivity, η_{melt} is dynamic viscosity, m is the exponent of reduction, θ is crystal fraction, and Ra is the Rayleigh number based on melt viscosity. This scaling suggests that a crystal fraction of 0.64 is a reasonable high-end estimate (Fig. 1). Equation 3 therefore shows that the regime change from zero crystal settling to efficient sedimentation occurs just below the value of critical packing in the vicinity of θ_o. Although other parameters play a role, the singularity in the two-phase viscosity function at $\theta = \theta_o$ serves as the

dominant predictor. A discussion of the derivation and considerations for estimating the catastrophic crystal loading fraction are provided in the Supporting Information file.

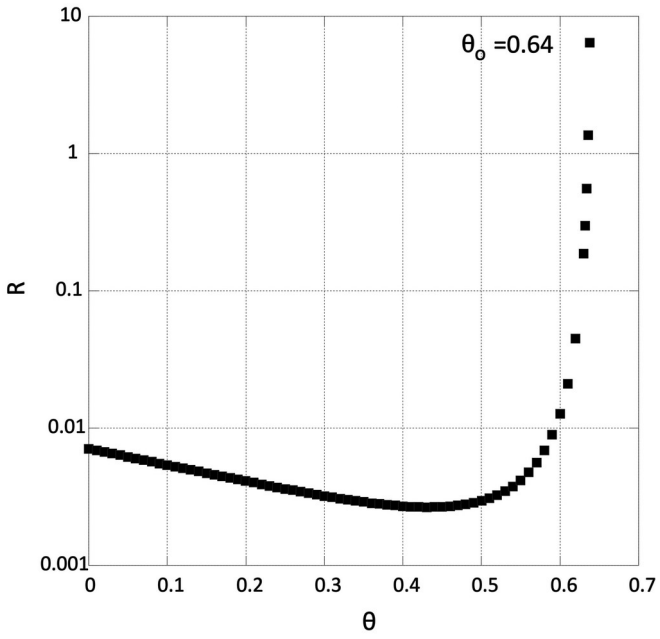

Figure 1. Dimensionless *R*-value represents a settling-to-convective RMS velocity ratio. Here the catastrophic solid fraction is $\theta = \theta_o = 0.64$.

While crystallization along the entire depth of the LMO column is possible, an adiabat need not lie perfectly parallel to the liquidus (Tonks and Melosh, 1990; Spera, 1992), and cooling may occur throughout during early convection due to efficient heat loss through the free surface. To simulate the petrological evolution of the LMO as it cools and crystallizes, stable phase assemblages were calculated for discrete spherical shells over the 1400-km depth. For the equilibrium crystallization portions of the models (Stage 1 in Fig. 2), mineral and melt characteristics were predicted over 1 to 45,000 bar, in ~2500-bar thick shells (18 total shells), along two adiabats that represents ~50% or ~60% solid. Each shell's equilibrium phase assemblage was estimated using the shell's mean *P* and *T*. The solids were then assumed to settle to the core-mantle boundary and incorporate 3% trapped melt, which is within the range suggested by Snyder et al. (1992). These cumulates represent the initial deep mantle and the new LMO-cumulate interface served as the base above which subsequent fractional crystallization occurred (Stage 2 in Fig. 2). A new LMO bulk melt composition was then computed.

Stage 2 equilibrium phase assemblages were calculated for the new LMO depth range in ~1000-bar thick shells, the exception being the uppermost shell that included any remaining LMO in a <1000-bar thick shell. The first adiabat was chosen based on the new thermodynamic melt properties determined by Perple_X such that <~3 vol.% LMO solids were produced. The solids were then dropped onto the existing cumulate mantle pile along with 3% trapped melt, thus building upward the cumulate mantle front. A new LMO bulk melt composition was then computed for the next fractional crystallization layer and a new adiabat determined from the new thermodynamic melt properties that produced <~3 vol.% LMO solids. This process repeated

until the LMO was fully solid. Perple_X output was used to track phase volume, composition, and density.

During the fractional crystallization stages, solid-melt density contrasts determined if crystals float or sink. Plagioclase has often been treated as a persistently buoyant phase during lunar crust formation (e.g. Elkins-Tanton et al., 2011; Johnson et al, 2021), adding to crustal thickness by underplating which progressively lowers the upper pressure-depth boundary. If our models produced a late-stage, silica-rich LMO melt at the base of the crust, any co-crystallizing plagioclase may not float or separate efficiently. However we considered the possibility of both scenarios, regardless of solid-melt density contrast, in order to compare the results to previous works. Model closure occurred when the combined total thickness of the floated plagioclase crust and the cumulate mantle equaled 1737.15 km and the LMO was fully solid. Layer thicknesses were calculated based on 3-D spherical volumes. Figure 2 shows the sequence of the two-stage 50% model, general characteristics, and expected phases with respect to a ~200-million-year solidification period (Maurice et al., 2020; as an example for a long-lived LMO) and LMO vol.% solidification. Table 1 contains starting parameters and parameter abbreviations for both the EQX50 and EQX60 models.

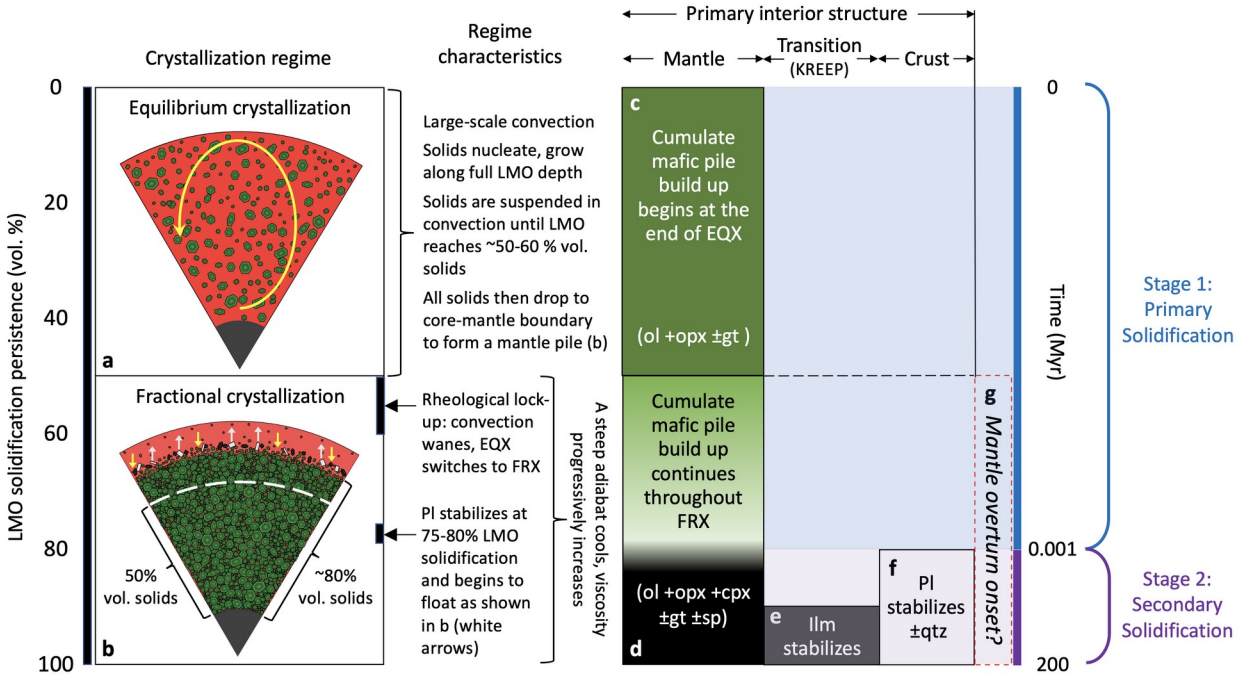

Figure 2. A schematic of the two-stage 50% LMO model. EQX = equilibrium crystallization, FRX = fractional crystallization. **c** and **d** show expected stable phases formed during the stages, the darker lower portion of **d** signifying the first appearance of cpx. Ilmenite forms late in LMO cooling (**e**), and a stagnant plagioclase lid (**f**) begins to form shortly before the first appearance of ilmenite. **g** represents the timing for a cumulate mantle overturn that can only begin after completion of **a**. Yellow and light gray arrows in **b** represent the simultaneous sinking of late-stage mafic phases and ilmenite and the floatation of plagioclase, respectively. The KREEP-rich transition zone (K, rare earth elements, and P) represents a residual LMO rich in incompatible elements and does not have a distinct boundary. Here the zone is associated with the appearance

of ilmenite. pl = plagioclase, ol = olivine, opx = orthopyroxene, cpx = clinopyroxene, gt = garnet, sp = spinel, qtz = quartz (or other silica phase).

Table 1

Parameters for initial conditions

Description	Symbol	Value
Bulk silicate Moon composition[a]	BSMC (LPUM)	wt.% oxide
SiO_2		46.1
MgO		38.3
FeO		7.62
Al_2O_3		3.93
CaO		3.18
Cr_2O_3		0.5
TiO_2		0.17
Na_2O		0.05
K_2O		0.003
Mean lunar radius[b]	R_{FULL}	1737.15 km
Mean core radius[c]	R_{CORE}	330 km
Depth-dependent LMO radius	r	< 1737.15 km
Full lunar volume	V_{FULL}	2.1958×10^{10} m^3
Core volume	V_{CORE}	1.5053×10^{8} m^3
LMO full volume	V_{LMO}	2.1808×10^{10} m^3
Gravitational constant	G	6.674×10^{-11} m^3 kg^{-1} s^{-2}
Mean lunar density[b]	ρ_M	3345.56 kg m^{-3}
LMO heat capacity[d]	Cp	EQX50: 357.08 J K^{-1} EQX60: 313.37 J K^{-1}
LMO thermal expansivity[d]	α	EQX50: 7.0775×10^{-5} K^{-1} EQX60: 7.1982×10^{-5} K^{-1}
LMO specific volume[d]	V	EQX50: 6.8483 J bar^{-1} EQX60: 6.1947 J bar^{-1}
LMO base pressure[e]	P_{BASE}	45000 bar
LMO base temperature[d]	T_{BASE}	EQX50: 2044 K EQX60: 1994 K
LMO surface pressure	P_{SURF}	1 bar
LMO depth	Z_{LMO}	1407.15 km
Adiabat[d]	dT/dP	EQX50, EQX60: ~28 K/GPa

[a]Longhi (2006). [b]Williams et al. (2014). [c]Weber et al. (2011). [d]Derived from Perple_X; a single set of values are used for the equilibrium crystallization portion of the models, and again recalculated at the

onset of each fractional crystallization layer. [e]Approximation derived from Eq. 1. ~~Parameters such as core radius and surface pressure remain constant.~~

3. Results

3.1. Equilibrium crystallization

The LPUM isochemical phase diagram (Fig. 3) shows the intersection of the garnet stability field with the EQX60 adiabat but not with the EQX50 adiabat, allowing garnet to crystallize at the base of the LMO during this stage. The curves represent total volumes of 50% and 60% equilibrium crystallization solids for the EQX50 (yellow line) and EQX60 (white line) models, respectively.

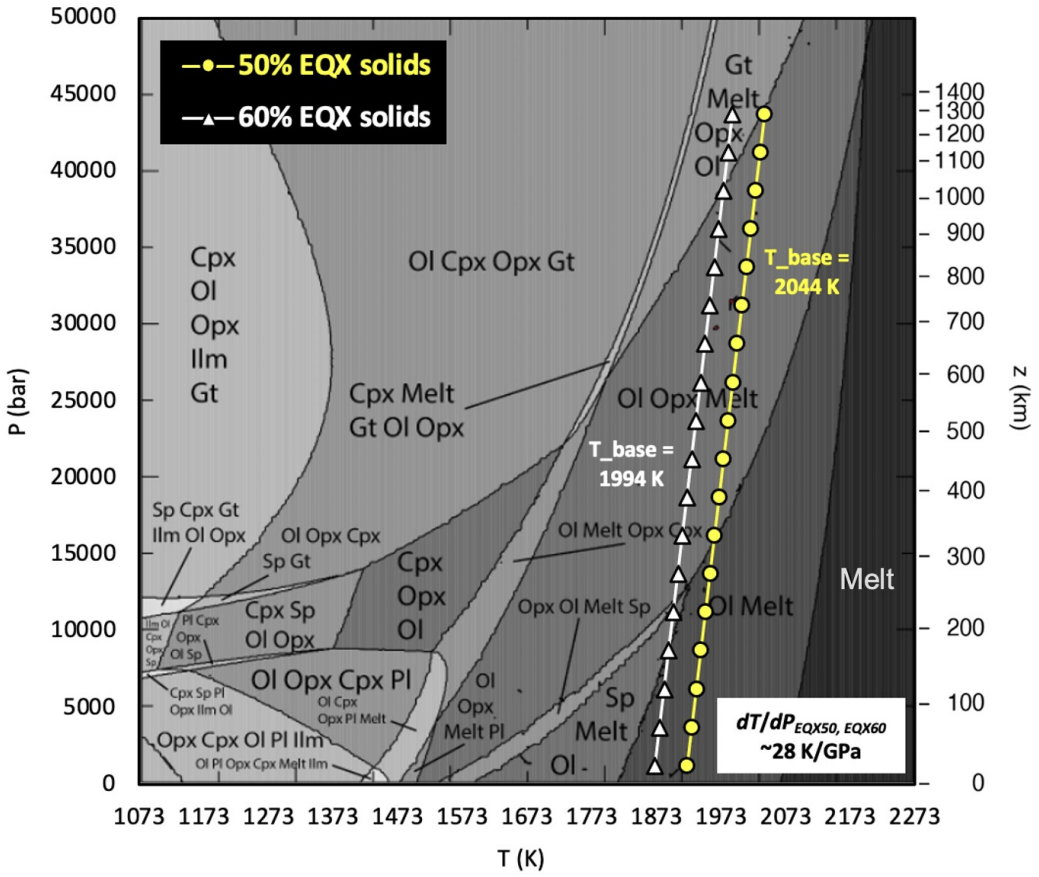

Figure 3. A pseudosection for the LPUM bulk silicate Moon composition over the range of pressures from the LMO surface to core-mantle boundary (~45000 bar) to approximately the lunar core center (~50000 bar). Both adiabats are steep and reflect an ~28K increase with every 1 GPa increase.

Our calculations show that EQX regimes produce mantles comprised of olivine (OL), orthopyroxene (OPX), and garnet (GT), with minor (0.03 vol.%) spinel (SP) stable only within a single shell at ~221 km-depth in the EQX60 model. The EQX50 model produced a cumulate mantle with a larger ratio of olivine to orthopyroxene (3.8) than the EQX60 model (2.7). Olivine

and orthopyroxene Mg# (= molar 100*[Mg/(Mg+Fe)]) ranged from 92-95 and 94-95 for the EQX50 and EQX60 models, respectively. For both models, orthopyroxene and olivine equilibrated toward the base of the LMO are less Mg-rich, more Fe-rich, and denser than those equilibrated toward the LMO surface due to the higher degree of solidification at higher pressures. Garnet in the EQX60 model stabilized at the LMO base and up through ~39000 bar (~1000-km depth). The amount produced in our models is small versus the full LMO volume but constitutes ~5 vol.% of the lower ~200 km of LMO solids.

We assumed a well-mixed mantle at the end of the EQX stage and estimated a bulk density based on the volumetric contributions of solid phases from each shell, all of which were denser than the melt environment. Similar bulk densities of 3150 and 3167 kg m^{-3} resulted for the EQX50 and EQX60 models, respectively. Without garnet, the EQX60 model bulk solid density was ~3155 kg m^{-3}. Figures 4 and 5 summarize these results, and Table 2 shows the three melt compositions (the starting LPUM, after 50% solids are removed, and after 60% solids are removed) with trends pointing to increases in all the LPUM components as equilibrium crystallization progresses, with the exception of MgO. Finally, the two models produce different cumulate pile heights, the surfaces of which rest at ~339 and ~259-km depth for the EQX50 and EQX60 models, respectively.

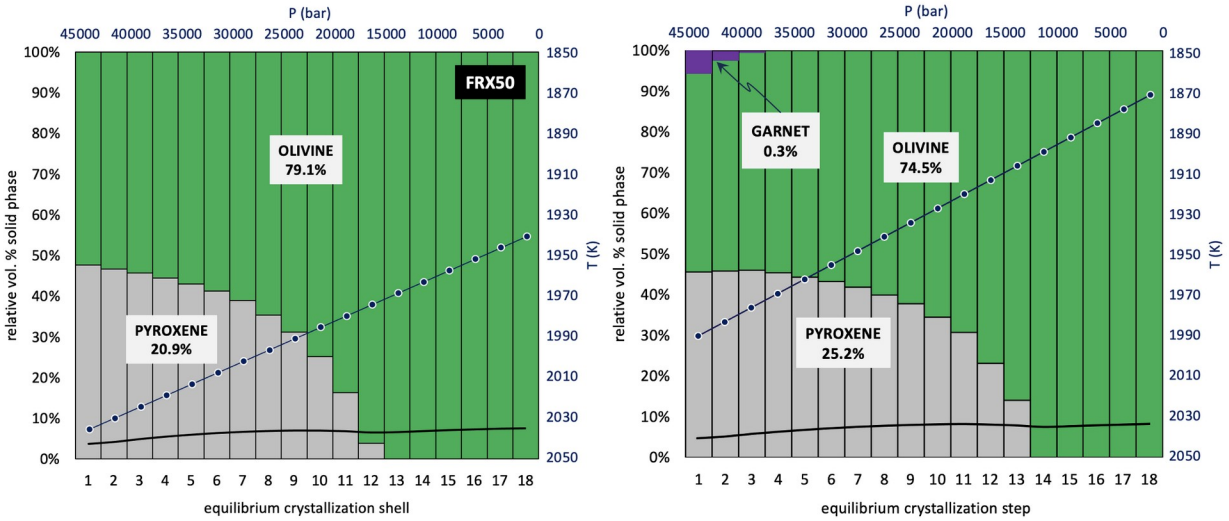

Figure 4. Relative vol.% of the three major solid phases that appear during the equilibrium crystallization stages of the two models, as a function of 18 shells. The blue line with circle markers represents the temperatures used for each shell's *P*-*T* calculation and corresponds to the red vertical axis on the right. The black curve represents the vol.% solids produced by each shell along the adiabat.

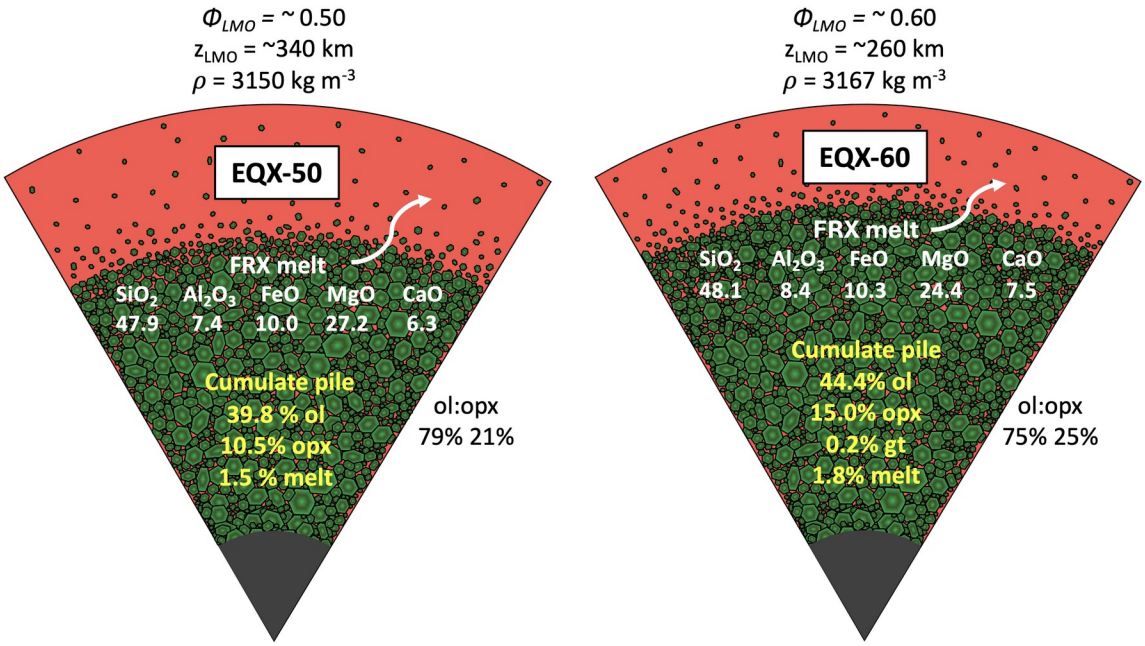

Figure 5. Schematic of key differences between early equilibrium crystallization characteristics of the two models. ϕ = crystal fraction of the LMO solidified. Cumulate pile bulk mineralogy and trapped melt percents (versus the full LMO) in yellow text, bulk residual LMO melt composition (FRX melt) wt.% is in white text.

Table 2

Bulk compositions (wt. %) of equilibrium crystallization melts and solids

Stage	SiO_2	Al_2O_3	Cr_2O_3	TiO_2	FeO	MgO	CaO	Na_2O	K_2O	Mg#
Start (LPUM)	*46.100*	*3.930*	*0.500*	*0.170*	*7.620*	*38.300*	*3.180*	*0.050*	*0.003*	*90*
EQX50 end melt	47.901	7.365	0.761	0.345	10.010	27.184	6.328	0.100	0.006	83
EQX60 end melt	48.113	8.373	0.763	0.415	10.271	24.424	7.512	0.122	0.008	81
EQX50 bulk solid	44.586	0.730	0.260	0.006	5.401	48.776	0.238	0.003	0.000	94
EQX60 bulk solid	44.965	1.096	0.331	0.013	5.940	47.238	0.409	0.004	0.000	93

Figure 6 compares the LMO melt composition at the end of the EQX stages from this work against four others all using LPUM but different convective regimes, LMO starting depths, and crystallization *P-T* paths: 1) Elardo et al. (2011) used an experimental approach considering four different pressures (1, 2, 3, and 4 GPa) and melt fractions from 20% to 75% for a 1400-km deep LMO; 2) Charlier et al. (2018) experimentally modeled the cooling of a 600-km deep LMO using a purely fractional crystallization model considering five different pressures from 0.08 to 1.20 GPa; 3) Rapp and Draper (2018) also created a fully fractional model but for a ~1400-km deep LMO over eight different pressures from 0.5 GPa to 4 GPa; and Johnson et al. (2021) employed computational phase equilibria to simulate a solidifying 1400-km deep LMO, using 50 mol.% as a proxy for 50 vol.% in attempting to reproduce the work of Elardo et al. (2011).

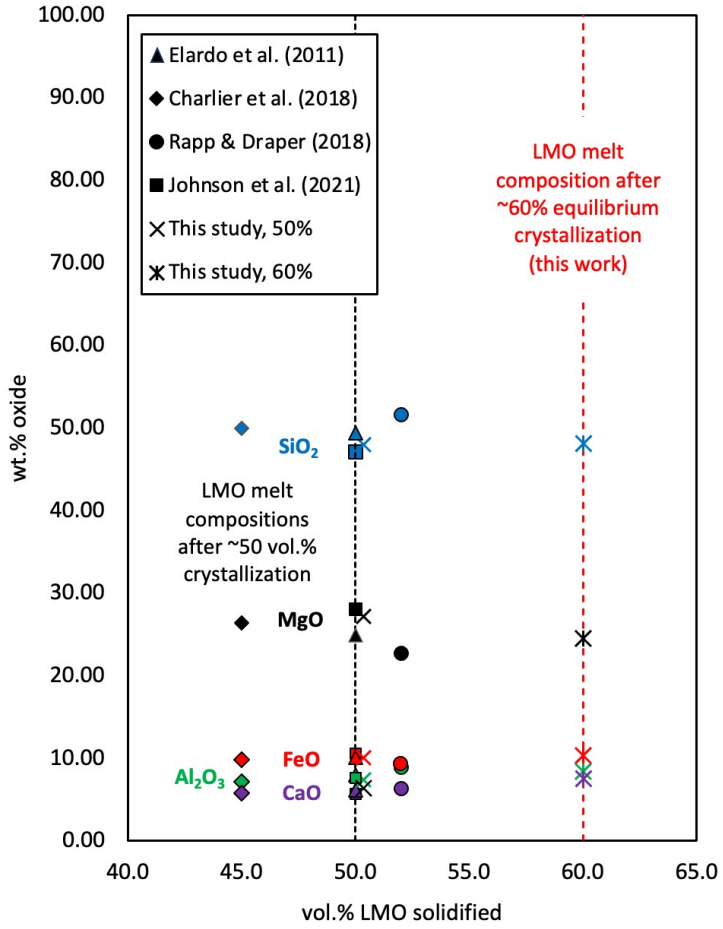

Figure 6. A comparison of published LMO melt compositions across works that considered an LPUM bulk silicate Moon, after ~50 vol.% solids are precipitated. Charlier et al. (2018) and Rapp and Draper (2018) used a fully fractional crystallization model whereas the others employed a two-stage model.

3.2 Fractional crystallization

3.2.1 Evolution of melt composition

The two fractional crystallization regimes of the EQX50 and EQX60 models (FRX50 and FRX60, respectively) produce similar melt composition trends (Fig. 7): SiO_2 increases with increasing formation of solids while FeO, Al_2O_3, and CaO steadily increase until plagioclase saturates at ~77-78% solids, at which point CaO and Al_2O_3 decrease and FeO increases further. At ~96-98% solids, the LMO is quartz saturated and FeO concentrations sharply decrease. Although the melt compositions of the two models trend similarly with respect to the cumulative volume of LMO solids produced, the trends may be offset by depth (e.g. peak melt FeO content occurs at ~77-km depth in the EQX50 model whereas in the EQX60 model, the peak value occurs at ~73 km). Inflections near 50% and 60% volumes are a result of the abrupt transition from equilibrium to fractional crystallization inherent in the models.

The last three shells of melt (the last shell being frozen in place immediately under the crust) in both models reflect melt densities that should inhibit efficient plagioclase flotation (plagioclase would be neutrally to negatively buoyant). This point is later discussed in context of crustal properties.

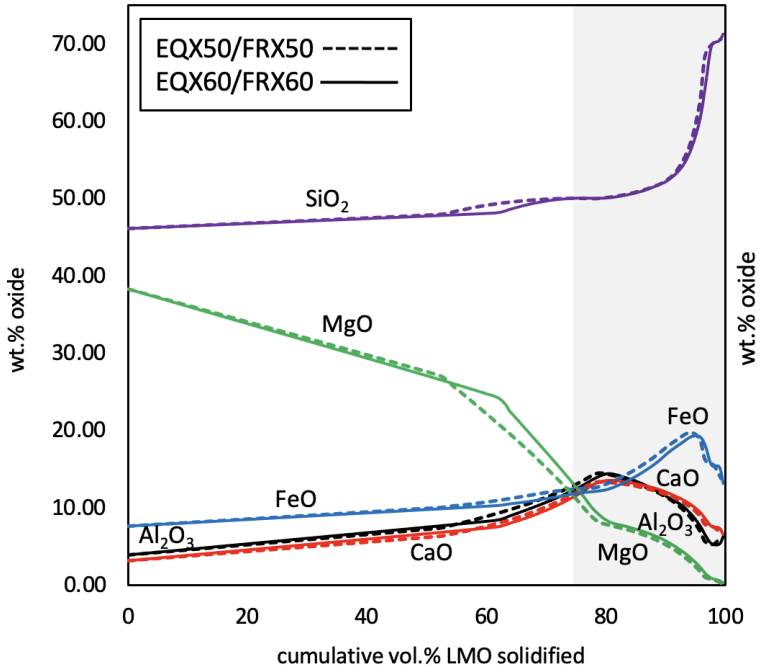

Figure 7. Compositional melt evolution as a function of LMO vol.% solidification. Melt composition curves for the full model, where the last step is frozen in place. The shaded area represents 75% to ~100% LMO solids, emphasizing element trends after plagioclase has stabilized.

3.2.2 Solid phase characteristics

Figure 8 shows the proportion of solid phases formed within each of the vertical depth-based packets of the FRX portions of the models (i.e. before crystal fractionation). Figure 9 shows relative mineral abundances and their depths after crystal fractionation. Orthopyroxene (opx) initially co-crystallizes with olivine, and opx proportions increase until clinopyroxene (cpx) stabilizes, at which point opx decreases and cpx increases. Ilmenite appears in both models over similar mantle layer thicknesses (~32 km), but at different depths (ilm in FRX50 settles to a depth of ~93 km and to ~88 km in FRX60). The volumetric contribution for both models is 0.11% versus V_{LMO} and is also similar at 2.1-2.2 vol.% versus the KREEP layer in which it resides. Spinel is dispersed over a thicker portion of mantle in FRX50 (~123 km) versus FRX60 (~75 km) and also at a greater depth in the former (~280 km versus 223 km). A second appearance of olivine occurs at ~98-99 vol.% LMO solids and is volumetrically greater in FRX60 (Fig. 7, labeled OL_U). For both models, sanidine only appears in the very last sub-crustal layer, and quartz contributes to the bottom 11-12 km of the crust. In general, the lower portion of FRX shells are ol and opx rich whereas the upper portion is cpx rich. Both models produce similar thicknesses of cpx+ilm-bearing mantle (82-84 km) and the first appearance at depth-of-settling is 144 km versus 137 km in FRX50 and FRX60, respectively.

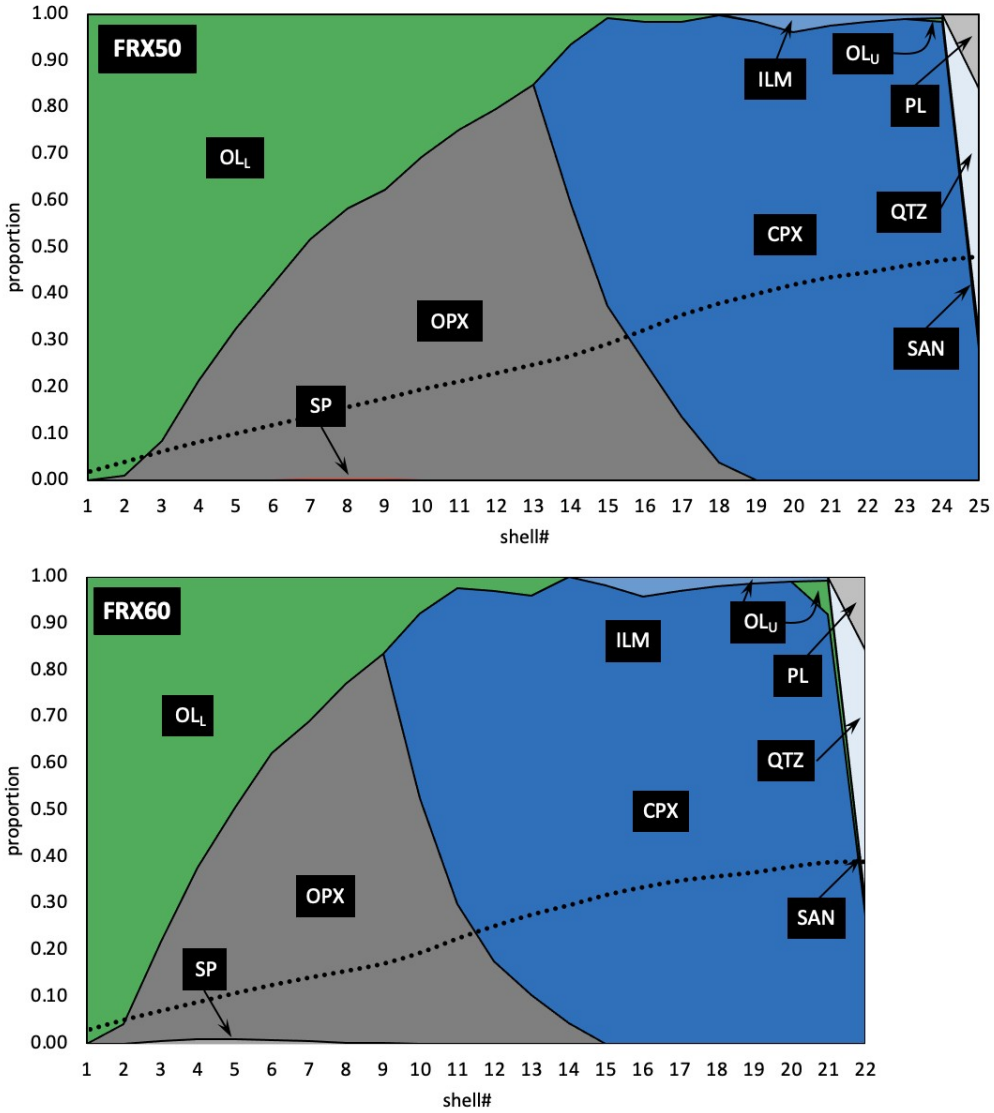

Figure 8. Mineral proportions per shell for each model where FRX50 has 25 layers and FRX60 has 22 layers (the crust is omitted here). The black dotted line represents the cumulative percent of LMO solids as a function of increasing shell# where shell# 1 is the FRX base and the highest numbered shell is the final, immediately sub-crustal shell that freezes in place.

The most significant difference thus far between the FRX portions of the models is the depths at which minerals settle or at which plagioclase-melt density contrasts first become apparent – although so far we treated plagioclase as efficiently floating throughout fractional crystallization (as have previous works) we then considered plagioclase that eventually becomes neutrally to negatively buoyant (Fig. 10). In FRX50, this density inversion occurs at 71 km below the LMO surface whereas in FRX60, the same inversion occurs at 64-km depth. Such a scenario has implications for lower crust mineralogy and density as well as for compositional variations in the very upper portions of the mantle (Fig. 11).

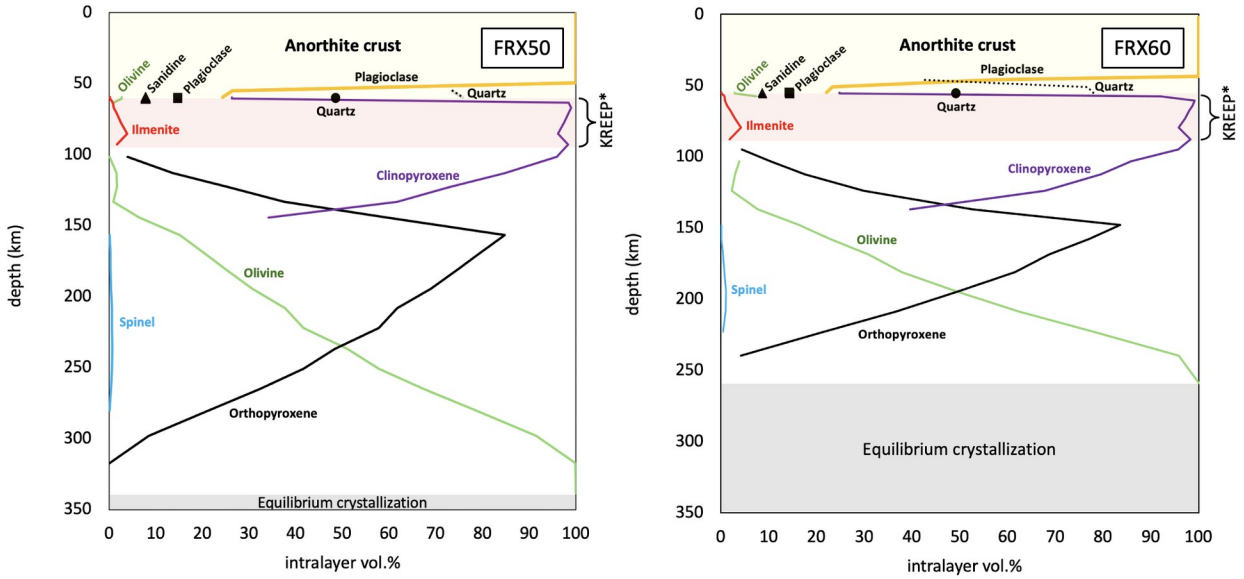

Figure 9. FRX50 and FRX60 plots showing the relative solid phase distributions as a function of depth. A potassium feldspar phase (sanidine) appears only in the last step of fractional crystallization where the remaining LMO (<1%) is frozen in place immediately under the crust. Markers for plagioclase and quartz indicate their occurrences in the last layer crystallized.

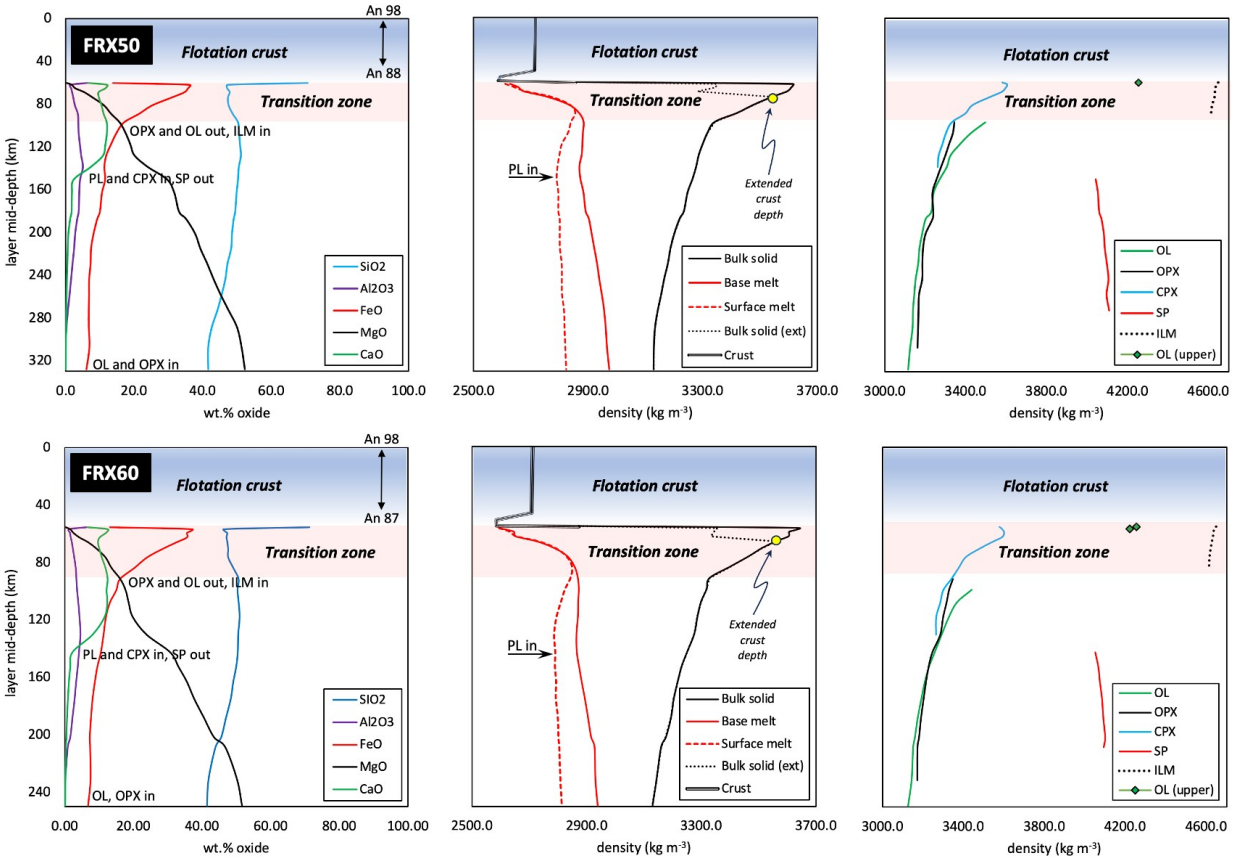

Figure 10. Upper mantle and crust characteristics. Left column: major element composition. Center column: density profiles of the mantle, the crust, and the melts at both the base and surface of each FRX step in which the solids first crystallized. Here quartz is incorporated with plagioclase as basal crust. Right column: density profiles of typically non-buoyant minerals after settling. Bulk solid (ext) = density profile if plagioclase is treated as negatively buoyant, as predicted in Perple_X. Yellow dots represent the approximate depths to which negatively buoyant plagioclase sinks. An = molar 100 × (Ca/(Ca+Na)). Quartz density remains constant at ~2551 kg m^{-3} (not shown).

In terms of general density trends, both models produce mantle densities that increase at a roughly linear rate with progressive crystallization toward the LMO surface, increase again at the base of the transition zone and then sharply decline at the upper transition zone due to the presence of quartz. The crusts are predominantly anorthite with ~1-km thick section that include plagioclase An_{87-88} and ~10-12 vol.% quartz (Fig. 12). Between this section and the anorthite are quartz-rich layers (~50 vol.%) ~10-11-km thick. Variations in plagioclase densities are minor (~2703 to 2715 kg m^{-3}). The complete EQX50 model results in a crust that is ~5 km thicker than that produced by the EQX60 model (61 km versus 56 km).

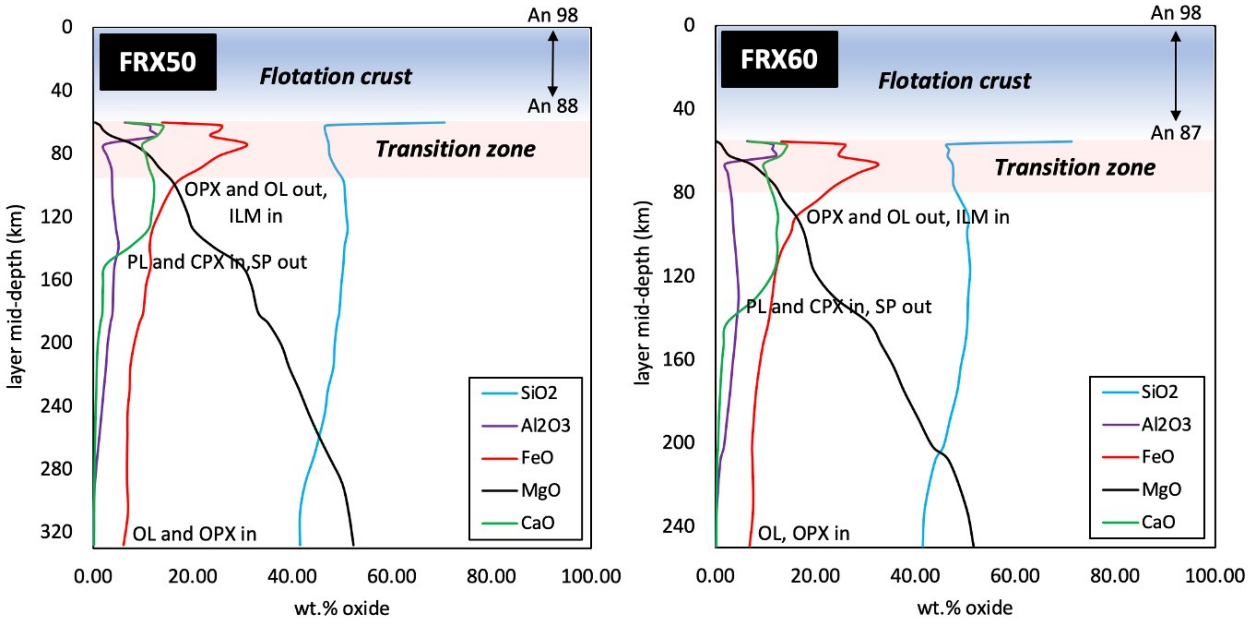

Figure 11. Bulk solid compositions of the upper mantle reflecting late-stage plagioclase sinking.

Current seismic models suggest a largely uniform mantle density from ~80 km down to ~1200 km and a crust that increases in density with depth (e.g. Garcia et al. 2019; Weber et al., 2011). Well-mixed equilibrium crystallization regimes produce initially uniform mantle densities by default (here ~3150-3170 kg m^{-3}) but less than that of Weber et al. (2011; ~3400 kg m^{-3}). Both models produced crustal thicknesses well in excess of current geophysical estimates. However, given that the nearside-derived GRAIL-era estimate of a 34–43-km thick crust relied in part on assumptions of physical characteristics of two specific nearside locales, a more accurate global thickness remains to be evaluated after a farside geophysical assessment by the Seismic Suite (FSS) experiments at the South Pole-Aitkin basin (Panning et al., 2022).

For mantle depths down to ~80 km, Wieczorek et al. (2013) predicted densities from 3360–3150 kg m^{-3} assuming uniform upper mantle porosity (they argued that a deeply impact-fractured crust may also have a fractured upper mantle). Our models produce greater mantle densities (~3400-3600 kg m^{-3}) down to ~80 km but match the Wieczorek et al. densities at greater depths (from ~100 km to > 200 km). This mismatch, along with density increases in Fe-bearing solid phases during progressive LMO solidification, provides further evidence for a cumulate mantle mixing event.

Garcia et al. (2019) noted a low velocity zone at depths from 100–250 km, potentially caused by proximity to heat producing KREEP. We note that this region strongly overlaps with the FRX60 lower boundary at ~260-km depth, up to the base of the transition zone (the latter serving as a KREEP layer analogue) at ~100 km. Our models show that this region could be interpreted as an initially lower-velocity one, at least relative to the overlying IBC/transition layer. Determining if the base of such a low-velocity zone could represent a relict equilibrium-to-fractional crystallization interface or even survive a cumulate mantle overturn (CMO) requires further investigation.

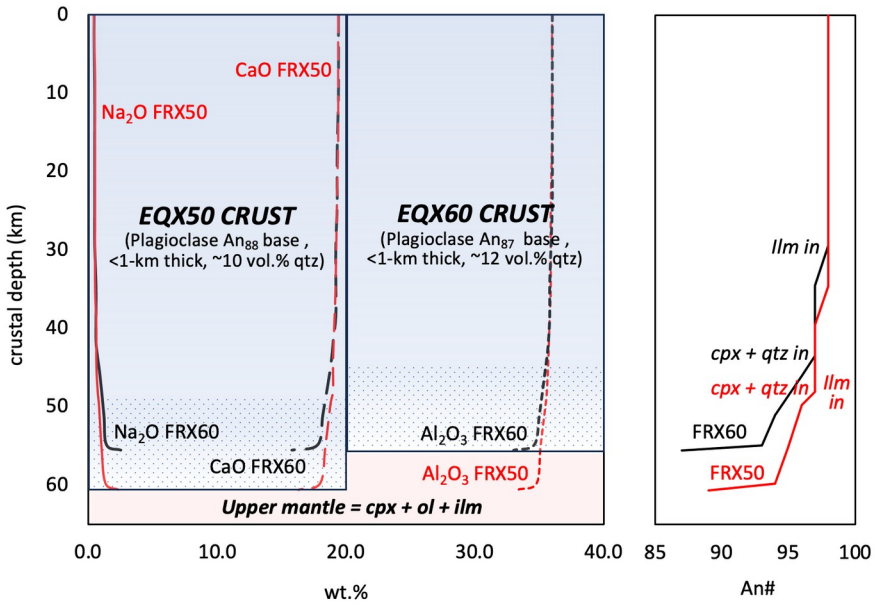

Figure 12. Schematic of the crust portions of the models. Lower dotted region indicates the presence of quartz.

The two models presented here reflect fully solidified, pre-overturn, ancient lunar interiors composed of four density and composition sub-structures: 1) an ol>opx lower cumulate mantle of largely uniform density and randomized distribution of early-formed mafic phases with Mg# > 90; 2) a stratified upper mantle of ol>opx≈cpx>sp that increases in density toward the transition zone; 3) a cpx+ilm transition zone that further increases in both density and FeO concentration toward a quartz-rich, low-density, base crust; and 4) a mostly uniformly dense, high-An bulk crust ($An_{97–98}$). We underscore that while density and composition trends are similar between the models, the major inflection points in these trends occur at different depths.

The depth at which fractional crystallization (i.e. the rheological transition) begins constrains the initial thickness, density, and composition of the bulk lower mantle. In this case, bulk lower mantle densities vary only slightly (the EQX50 lower mantle is 3150 kg m^{-3} versus 3167 kg m^{-3} for the EQX60 model), and the residual LMO is slightly more Mg-enriched in the former by ~3 wt.%. The KREEP-bearing transition zones are similar in thickness and composition but occur over different depths. The crust is 5 km thinner in the EQX60 model yet given the current estimate of a 34-43 km lunar crust, the difference may not be insignificant. Garnet appears in the EQX60 model's basal mantle but not in the EQX50 model.

4. Discussion

We compare our two new models against previous results that also used a LPUM bulk silicate Moon composition (Fig. 13). While these models consider both shallow and deep magma oceans, two-stage to purely fractional crystallization, and a range of crustal thicknesses and cumulate mantle stratigraphies, here we focus on key differences and similarities that stem from a change in crystallization regime switching (i.e. EQX50 vs EQX60).

4.1. Implications for crustal thickness and composition

In both of our new models, solid-melt density contrasts suggest that plagioclase should sink or stagnate in the late stages of crustal underplating. In the EQX50 model, stagnation would initiate at ~70 km and in the EQX60 model, at ~64 km. This density inversion has potentially two major effects: 1) increasing alumina concentration in the upper mantle from 1-2 wt.% to 11-13 wt.%, and 2) reducing lower crust density by introducing a quartz-rich residuum. However, previous LMO models have generally defined the lunar crust as constructed by plagioclase that remains persistently and positively buoyant throughout formation. If solid-melt phase density contrast is the primary mechanism for building the Moon's anorthositic crust, this implies that most published two-stage models have not adequately addressed the effects of a late-stage, low density melt on crustal formation, even in those that produce late-stage silica-rich melts (e.g. Charlier et al., 2018; Johnson et al., 2021). Sub-crustal quartz should be identified by reduced seismic wave speed signatures near the base of the crust; however, it may alternatively have been displaced and/or re-equilibrated with other crystallization products during mantle overturn. If physically mixed with an upper mantle of mafic-dominated composition, the lower crust-upper mantle may be divided by a transition zone yielding seismic signatures closer to that of a plagioclase-dominated crust.

No returned samples or lunar meteorites have indicated the presence of a sub-crustal LMO-derived quartz layer, suggesting that if it formed during LMO crystallization, it has since reacted away. Any primary quartz found on the lunar surface would have to had survived excavation via a large impactor such as the one that created the South Pole-Aitkin basin (e.g. Melosh, 2017). Even if excavated quartz survived the heat of such a large impactor, having been sourced from greater depths (e.g. Hurwitz and Kring, 2014), the quartz ejecta would then need to have survived melt sheet temperatures potentially in excess of that for quartz melting (~1650°C). While speculative, we consider that only minor amounts of quartz were originally excavated, and subsequent impact gardening combined with higher melt sheet temperatures obliterated or obscured obvious traces of any primary quartz on the lunar surface. ~~Ti-in-quartz~~

~~thermobaromtery coupled with, for example, computational phase equilibria constraints on Ti-saturation at depth could help elucidate the formation depths of lunar quartz.~~

In general, deep-LMO models (>1000 km) tend to produce crusts with thicknesses in the range ~50-60 km, significantly thicker than GRAIL-based estimates of 34-43 km. If plagioclase that crystallized from an LMO stagnates or sinks, as suggested in both our models, it may (a) sink so slowly that it becomes part of an extended crust with quartz and minor mafic components, or (b) sink quickly enough to form a separate plagioclase-rich layer. In the latter, the proper flotation crust would be ~48-km thick in the EQX50 model and ~43-km for the EQX-60 model, and a quartz- or silica-rich layer mixed with negatively buoyant plagioclase below would largely be unpreserved after a CMO initiated from a dense ilmenite-bearing cumulate (IBC). Our findings suggest that extended equilibrium crystallization of the LMO is one possible pathway to achieve a crustal thickness more in alignment with the GRAIL-based range, and that a thin lunar crust by itself would not necessarily imply the presence of water, which delays plagioclase crystallization (e.g. Lin et al., 2020). The findings also highlight the need for further investigation into the environmental conditions would have been in place just after the Moon-forming impact to promote a prolonged period of LMO crystal suspension.

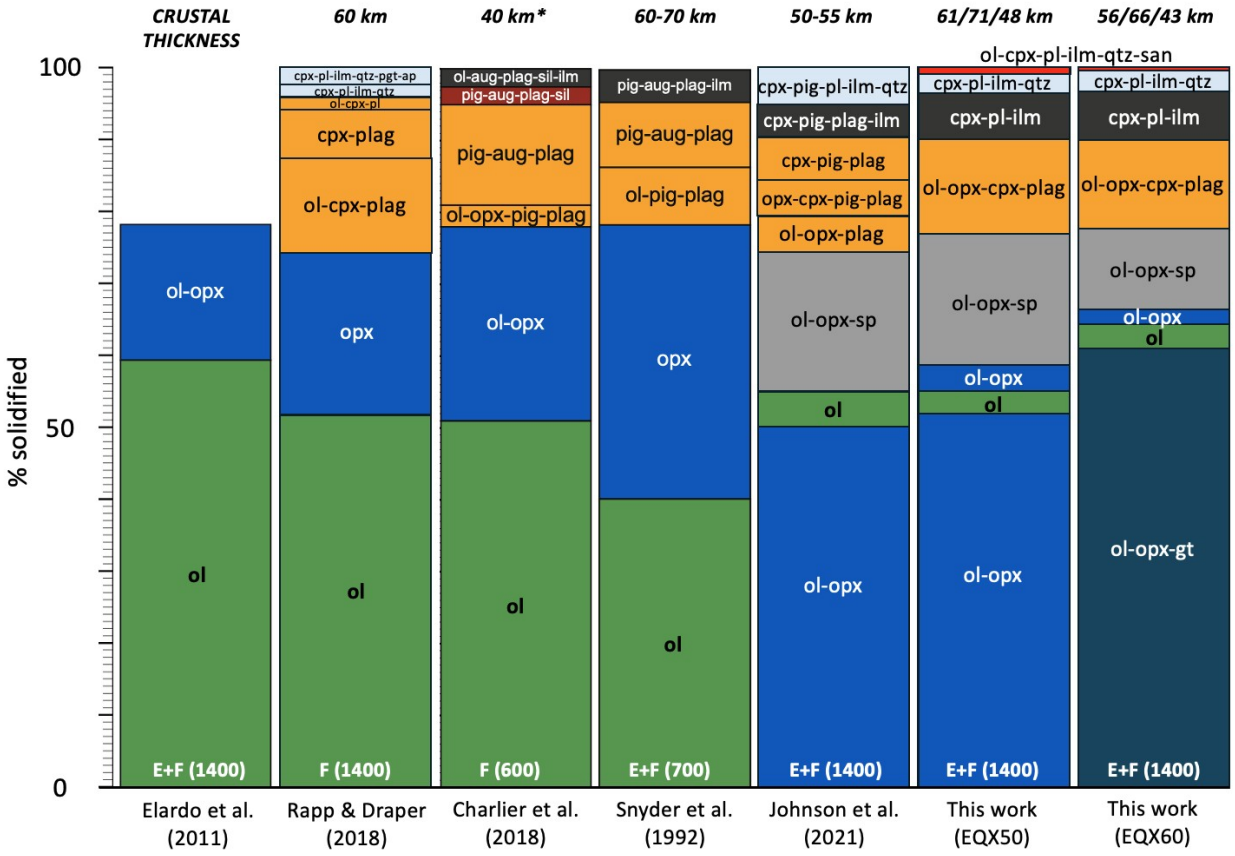

Figure 13. Modified from Charlier et al. (2018). A comparison of phase appearances as a function of % LMO solidified. Pig = pigeonite, a low-Ca variety of cpx, has been left as a separate pyroxene species when indicated as such by the original work. E+F = the two-stage model, F = fractional crystallization. Numbers in brackets indicate the LMO depth that was modeled. * = one value within an approximate range of 40 ± ~5 km. For EQX50 and EQX60,

the first of three values = all plagioclase is floated; second value = late-stage plagioclase stagnates to form an extended crust; third value = a crust of only positively buoyant plagioclase.

4.2. Differences in early cumulate pile solids from differences in approaches

Not all full-depth LMO LPUM models produce the ~~Al-bearing phase~~ orthopyroxene during initial convection. For example, our two new models, as well as those from Johnson et al. (2021), produce orthopyroxene early in the crystallization sequence, leaving less Al for later-formed plagioclase. The experimental works of Elardo et al. (2011) and Rapp and Draper (2018) both considered LMO base crystallization conditions in the range of ~1800°C at 4 GPa, and neither model produced orthopyroxene. The cause of discrepancies between these calculated phase equilibria and experimental models is unclear, and highlight that predictions about the composition and petrology of Moon's pre-overturn cumulate mantle are highly sensitive to model parameters and methodological choices.

The EQX60 model produced ~5% more Al-bearing orthopyroxene than the EQX50 model. In general, orthopyroxene and/or olivine saturation dominate the early cumulate mantle in all these models (Fig. 13) and is likely the primary cause for a restricted range of crustal thicknesses, despite differences in model approach or method. The most direct comparisons can be made between our models and the LPUM model of Johnson et al. (2021), who also explored the TWM composition. Although both works use a computational phase equilibria approach for a two-stage LPUM model, different approaches were used for estimating the first 50% solids precipitated. While our work used key thermodynamic properties of the melt to define an adiabat for crystallization where 50% or 60% solids precipitated simultaneously, Johnson et al. (2021) chose a 50% solids path directly between and parallel to the liquidus and solidus, using mol.% as a proxy for vol.%. Consequently, a 50% equilibrium crystallization regime produced different phase proportions (~45 mol.% opx and 55 mol.% ol for Johnson et al., and ~20 vol.% opx and ~80 vol.% ol for this work). Such differences are potentially significant, yet often viewed as generally similar. For example, thermodynamic output for this work at P ~44000 GPa and T ~2040 K for an LPUM composition shows olivine at ~34 vol.% with an equivalent mol.% of 43. At surface P and T, olivine output is ~55 mol.%, or ~42 vol.%. How these differences eventually translate to a full model was beyond this scope of this work, with the larger issue being that untangling the effects of parameter choices and modeling approaches on results is not straightforward. Computational phase equilibria modeling does provide an efficient and inexpensive means for investigating planetary cooling, permitting inquiry into higher P-T space than some experimental techniques. For more robust results, computational methods should be combined with experimental verification, all using the same parameters when possible.

The appearance of garnet during the end of the equilibrium crystallization portion in the EQX60 model shows that an Earth-like BSMC is capable of producing minor amounts of garnet when convection is vigorous, and so an Al-enriched BSMC like TWM may not be required. The presence of garnet has been invoked to explain sound velocities and high seismic velocities in the Moon's lower mantle (Anderson, 1975; Weber et al., 2011; Wood et al., 2024). Bhanot et al. (2024) found potential relict garnet signatures in the form of Cr-spinel+olivine symplectites that may once have been olivine+Cr-garnet, stirred up from the base of the mantle during an overturn

event. We therefore consider garnet to be a likely part of the lunar mantle, and this may have formed due to extended convection.

4.3. Cumulate pile fronts and the IBC layer: potential effects on a mantle overturn

LMO models inevitably produce ilmenite as LMO solidification proceeds, and with continued ilmenite crystallization the LMO dregs eventually become Fe-depleted and silica saturated according to some models (Fig. 12). As ilmenite is considered a key component of the IBC which drove late-stage mantle mixing (i.e. CMO), its first appearance and volumetric distribution remain of interest. The CMO would have forced an exchange of material between the KREEP-bearing IBC layer and the high-Mg cumulate mantle pile below it. This exchange serves as a possible mechanism for enigmatic Mg-suite magmatism (e.g. Elkins-Tanton et al., 2002; Elardo et al., 2011; Prissel et al., 2023), rendering pre-CMO stratigraphy as a highly relevant.

For example, prolonged early LMO convection places the final cumulate pile height 80-km closer to the surface (~260 km versus 340 km for the two-stage EQX50 model). The first appearance of ilmenite in both models occurs at 90% LMO solids, similar to Johnson et al. (2021; and models referenced therein), earlier than the fully fractional LPUM model of Rapp and Draper (2018) at 97% solids, and slightly later than the relatively Fe-enriched (non-LPUM; 12 wt.% FeO) deep-LMO model of Elkins-Tanton et al. (2011) at ~88% LMO solids. The thicknesses of the IBC for both EQX50 and EQX60 models are similar at 58-59 km and ilmenite volumes also similar at 2.1-2.2 vol.%., the latter in general agreement with that of Elardo et al. (2011; ~3.6 vol.% ilmenite).

Our work supports the idea that full-depth, two-stage LPUM LMO models promote volumetrically low ilmenite production, consequently leading to shallow CMOs. However, the first appearance of ilmenite at the base of the cumulate pile front occurs relatively sooner (deeper) in the EQX50 model at a depth of ~93 km versus ~88 km in the EQX60 model, suggesting that extended LMO convection model could cause relative delay in the onset of a CMO. When coupled with a smaller separation distance (172 km versus 247 km) between the base of the IBC and the top of a well-mixed high-Mg cumulate mantle pile, extended convection provides a physically shorter path for accessing high-Mg cumulates. While the values above are particular to the parameter definitions of the two models, we underscore that the goal is to show potentially significant, systematic changes can result from small changes in early convective vigor. The volume of ilmenite that crystallizes, the thickness and viscosity of the IBC layer, and the rheology of the mantle at the time of overturn are all crucial aspects of the CMO that remain poorly constrained (e.g. Li et al., 2019).

4.4. Upper mantle composition

Melosh et al. (2017) suggested that the impact that created the 2500-km diameter South Pole-Aitkin (SPA) basin on the Moon's southern farside likely excavated the upper lunar mantle to depths of ~100 km. Combined with compositional remote sensing data, they concluded that the upper mantle is largely composed of low-calcium pyroxene (LCP). In both models in this work, clinopyroxene (mostly low-Ca augite) dominates upper mantle composition from ~100-km depth to the base of the crust, and negligible amounts of olivine are present. Other works have

concluded orthopyroxene-rich upper mantle sources, most recently from Chang'e-5 mission samples collected from the nearside in the northwest portion of the Procellarum KREEP Terrane (Sheng et al., 2024). However, spectral signatures on the lunar surface at different locales hint at different mantle lithologies – while Melosh et al. and Yamamoto et al. (2023) both concluded that LCP exposures dominate the SPA region, Yamamoto et al. also show that olivine is the dominant exposed mafic phase in other basins such as Crisium (nearside) and Moscoviense (farside). More likely, the lunar mantle is both laterally and vertically heterogeneous (as previously suggested by numerous works), whether induced by cumulate mantle mixing or by initially heterogeneous solidification processes, or both. The latter point goes back to the issue of the lunar crustal dichotomy – either the Moon's crust initially formed in a hemispherically-bound and variably-thick state or was preferentially thinned out on the nearside after formation.

4.5. Moving away from the spherically uniform LMO cooling model: a dichotomously solidifying Moon

One shared parameter across all two-stage and fully-fractionating LMO models is the assumption of a symmetrically and uniformly cooling LMO. Based on current estimates that combines gravity observations with nearside crustal measurements, the farside crust is markedly thicker (up to ~60 km) than the nearside crust (20–30 km) with a global mean thickness (34-43 km) similar to that of Earth (Wieczorek et al. 2013). Previous works have explored the potential origins for the lunar crustal dichotomy, ranging from radiogenic heat contributions (Elardo et al. 2020), to a large nearside impact (Zhu et al. 2019), and to the early influence of a hot Earth (Roy et al. 2014). Roy et al. proffered that a post-impact debris disk of 2000–10000 K would influence crustal thickness if the Moon became tidally locked early on, and Lock et al. (2020, 2018) suggested that a different hot post-impact Earth structure at an ~2300 K external disk temperature must affect lunar magma ocean cooling. In addition, reflectance spectra suggest that the farside crust may have evolved from more primitive magma, as evidence by a higher magnesium-to-iron ratio (Ohtake et al. 2012). This evidence reinforces the possibility that the Moon's crust may have initially formed in an asymmetric state.

Boukaré et al. (2022) offered a model for planetary cooling that captures the above, that a planet tidally locked to its sun could exist in a partially molten state with a solid region on the side facing away from the sun and a molten region on the sun-facing side. Given this model for paired tidal locking and crystallization, our model results, and the results of similar full-depth LMO works (e.g. Fig.12), we suggest the possibility that spherically uniform LMO solidification models may actually reflect generation of the Moon's farside crustal thickness than a global mean, accounting for some of the discrepancy between GRAIL-based estimates and model-predicted ones. This conclusion is drawn in part from the extreme differences in crustal thickness between the lunar farside (up to ~60 km) and the nearside (20-30 km) (Wieczorek et al., 2013). A lunar nearside tidally locked to hot post-impact Earth at the onset of LMO solidification would have endured surface temperatures initially hovering above the liquidus such that crystallization would be suppressed at depth and convection weak. Figure 14 shows such a scenario. Assuming that tidal locking occurs early, the Moon is outside the Roche radius, and the external disk temperature is >2300 K, the colder lunar farside crystallizes in a manner similar to the models in this work. The nearside experiences weaker convection as the temperature differential between LMO base and surface is initially small. There would be some communication between

hemispheres, but hemispheric differences in magma ocean depth and crystallization styles would be likely (Boukaré et al., 2022).

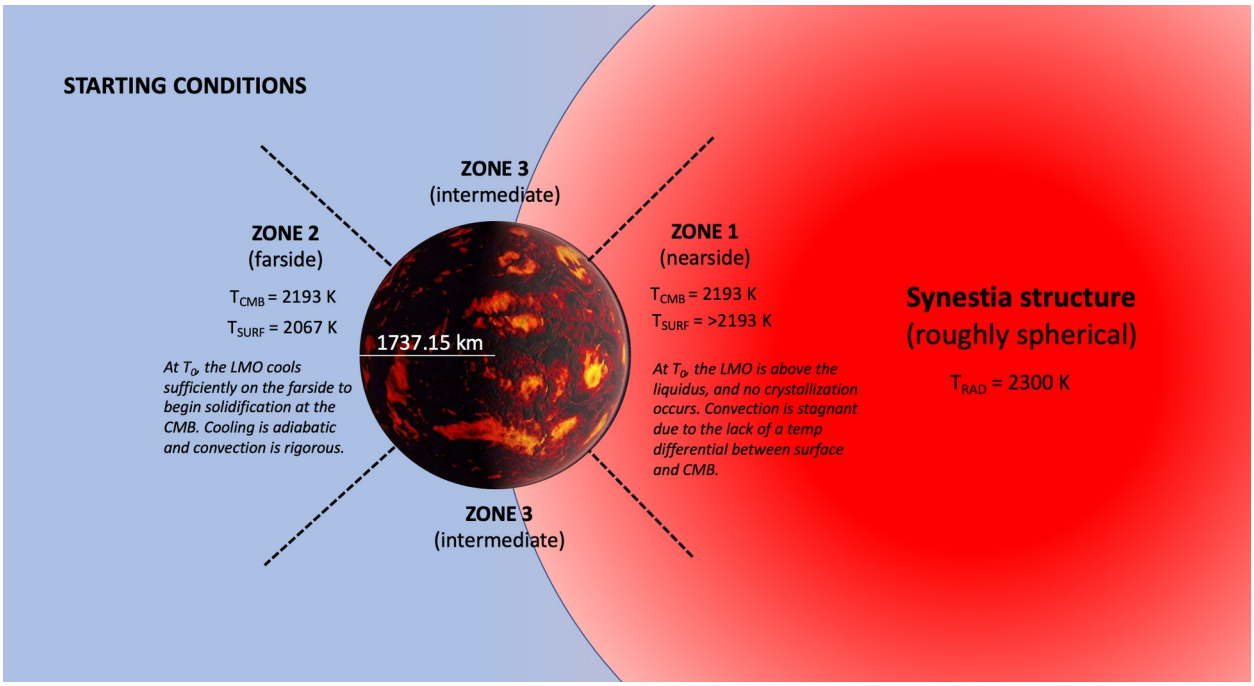

Figure 14. Schematic showing a dual cooling regime for an LMO with two different surface temperatures and similar core-mantle boundary (CMB) temperatures. The nearside surface temperatures are 1) approximately equal to internal mantle temperatures or 2) greater than internal mantle temperatures. Condition 2 will increase depression of the adiabat-liquidus intersection compared to 1, rendering convection minimal to negligible. We assume post-impact hot Earth effective geometries (based on the synestia model of Lock et al., 2020) are roughly spherical and are scaled at ~3.7x the radius of the Moon.

5. Conclusion

Variations in petrological structure determined from LMO models result from a combination of different approaches (i.e. experimental versus numerical), LMO parameters (e.g. LMO depth, *P-T* values for crystallization, model resolution), and assumptions about an initial thermal state. The general effects of varying some parameters may be arrived at more intuitively (such as increases in bulk FeO are likely to lead to increased ilmenite production and perhaps a denser late-stage melt) than others (i.e. the small changes in petrological layering forced by an increase in early convection). Without systematically varying model parameters, however, comparing results across multiple models becomes problematic. Even LMO model resolution (i.e. the number of shells or layers) can lead to differences in petrological structure. An extreme example would be the instantaneous freezing of the Moon (i.e. a one-shell approach). Reverting to an LPUM pseudosection (Fig. 3) to estimate the petrology and stratigraphy, there would be no plagioclase-dominant lithology serving as the pseudo-crust and garnet would occupy the lower ~1200 km of a coreless rocky body.

Whereas previous LPUM LMO works produce the first 50% solids as largely Mg-rich olivine and/or orthopyroxene with similar bulk densities, our models introduce the effects on early whole-Moon differentiation by extending the volume of early crystal suspension to a plausible 60% solids. The models suggest that garnet in the lunar mantle is possible without having to invoke an alumina-enriched BSM. This finding is not to be taken as proof or even likelihood of mantle garnet due to persistent early convection. Rather, we suggest that convective rigor coupled with, say, a minor increase in alumina may provide another means for creating mantle garnet.

LMO models that produce late-stage silica-rich melts must contend with the effects on plagioclase floatation. We find this consideration lacking in the literature. Current seismic interpretations of the lunar farside are based on nearside seismic data, and so future seismic missions will likely lead to reassessments of lunar crustal thickness, forcing re-examinations of previous LMO works. That a vigorously convecting LMO favors a thinner crust (among other traits) than conventional 50%-solid two-stage models is, to our knowledge, a novel finding that reinforces the importance of convective styles for modeling the building of small rocky bodies.

CRediT authorship contribution statement

Kim Cone: Writing – Original draft, Writing – Review and Editing, Conceptualization, Methodology, Formal Analysis, Visualization, Funding acquisition, Data curation. Stephen Elardo: Methodology, Review and Editing. Frank Spera: Methodology, Visualization, Writing – Original Draft, Writing – Review and Editing. Wendy Bohrson: Methodology, Writing – review and editing. Richard Palin: Conceptualization, Methodology, Resources, Writing – Review and Editing, Supervision.

Declaration of competing interest

The authors declare no competing interests. This research was conducted without any commercial or financial relationships that could be perceived as a potential conflict of interest.

Acknowledgments

The authors wish to acknowledge funding and support from the Geological Society of America through a GSA Graduate Student Geoscience Grant #13410-22 funded by NSF Award #1949901, and an NSF-supported IIE-GIRE Fellowship under Grant #1829436. We thank Andrea Distel at Arizona State University for assistance with editing.

Open Research

Supporting data for this manuscript are available via the EarthDataAlliance (IEDA) repository (https://... to be finalized post-submission).

References

Abe, Y. (1995). Early evolution of the terrestrial planets. Journal of Physics of the Earth, 43, 515-532.

Anderson, D.L. (1975). On the Composition of the lunar interior. Journal of Geophysical Research, 80, 148-227. https://doi.org/10.1029/JB080i011p01555

Bhanot, K.K., Downes, H, Rider-Stokes, B.G., (2024). A reappraisal of the petrogenesis of Apollo 17 lunar dunites.

Boukaré, C-E., Parmentier, E.M., Parman, S.W. (2017). Did lunar mantle ocean overturn before the end of magma ocean solidification? LPSC XLVII, abstract 2494. https://www.hou.usra.edu/meetings/lpsc2017/pdf/2494.pdf

Boukaré, C-E., Cowan, N.B., Badro, J. (2022). Deep two-phase, hemispherical magma oceans on lava planets. The Astrophysical Journal, 936, 9pp. https://doi.org/10.3847/1538-4357/ac8792

Canup, R.M., Asphaug, E. (2001). Origin of the Moon in a giant impact near the end of the Earth's formation. Nature, 412, 708-712. https://doi.org/10.1038/35089010

Canup R.M. (2004). Simulations of a late lunar-forming impact. Icarus, 168, 433-466. https://doi.org/10.1016/j.icarus.2003.09.028

Charlier, B., Grove, T.L., Namur, O., Holtz, F. (2018). Crystallization of the lunar magma ocean and the primordial mantle-crust differentiation of the Moon. Geochimica et Cosmochimica Acta, 234, 50-69. https://doi.org/10.1016/j.gca.2018.05.006.

Cone, K. (2021). ApolloBasalt DB_V2, Version Version 1.0. Interdisciplinary Earth Data Alliance (IEDA).

Cone, K.A., Palin, R.M., Singha, K. (2020). Unsupervised machine learning with petrological database ApolloBasaltDB reveals complexity in lunar basalt major element oxide and mineral distribution patterns. Icarus, 346, 113787. https://doi.org/10.1016/j.icarus.2020.113787

Costa, A., Caricchi, L., Bagdassarov, N. (2009). A model for the rheology of particle-bearing suspensions and partially molten rocks. Geochemistry, Geophysics, Geosystems, 10, 2785-2806. https://doi.org/10.1029/2008GC002138

Connolly, J.A.D. (2005). Computation of phase equilibria by linear programming: A tool for geodynamic modeling and its application to subduction zone decarbonation. Earth and Planetary Science Letters, 236 (1-2), 524–541. https://doi.org/10.1016/j.epsl.2005.04.033

Connolly, J.A.D. (2009). The geodynamic equation of state: what and how. Geochemistry, Geophysics, Geosystems, 10, Q10014. https://doi.org/10.1029/2009GC002540

Cuk, M., Stewart. (2012). Making the Moon from a fast-spinning Earth: A giant impact followed by resonant despinning. Science, 1047-1052. https://doi:0.1126/science.1225542

Dauphas, N., Burkhardt, C., Warren, P.H., Fang-Zhen, T. (2014). Geochemical arguments for an Earth-like Moon-forming impactor. Philosophical Transactions of the Royal Society A, 372, 20130244. https://doi.org/10.1098/rsta.2013.0244

Elardo, S.M., Draper, D.S., Shearer, C.K. (2011). Lunar magma ocean crystallization revisited: bulk composition, early cumulate mineralogy, and the source regions of the highlands Mg-suite. Geochimica et Cosmochimica Acta, 75, 3024-3045. https://doi.org/10.1016/j.gca.2011.02.033

Elardo, S.M., Laneuville, M., McCubbin, F.M, Shearer, C.K. (2020). Early crust building enhanced on the Moon's nearside by mantle melting-point depression. Nature Geoscience, 13, 339-343. https://doi.org/10.1038/s41561-020-0559-4

Elkins-Tanton, L.T., Van Orman, J.A.., Hager, B.H., Grove, T.L. (2002). Re-examination of the lunar magma ocean cumulate overturn hypothesis: melting or mixing is required. Earth and Planetary Science Letters, 196, 239-249. https://doi.org/10.1016/S0012-821X(01)00613-6

Elkins-Tanton, L.T. (2012). Magma oceans in the inner solar system. Annual Review of Earth and Planetary Science, 40, 113-139. https://doi.org/10.1146/annurev-earth-042711-105503

Elkins-Tanton, L.T., Burgess, S., Yin, Q-Z. (2011). The lunar magma ocean: reconciling the solidification process with lunar petrology and geochronology. Earth and Planetary Science Letters, 304, 326-336. https://doi.org/10.1016/j.epsl.2011.02.004

Elkins-Tanton, L.T. (2008). Linked magma ocean solidification and atmospheric growth for Earth and Mars. Earth and Planetary Science Letters, 271, 181-191. https://doi.org/10.1016/j.epsl.2008.03.062

Garcia, R.F., Khan, A., Drilleau, M., Margerin, L., Kawamura, T., Sun, D., et al. (2019). Lunar Seismology: An Update on Interior Structure Models. Space Science Reviews, 215. https://doi.org/10.1007/s11214-019-0613-y

Green, E.C.R., White, R.W., Diener, J.F.A., Powell, R., Holland, T.J.B., Palin, R.M. (2016). Activity–composition relations for the calculation of partial melting equilibria in metabasic rocks. Journal of Metamorphic Geology, 34, 845-869. https://doi.org/10.1111/jmg.12211

Hart, S.R., Zindler, A. (1986). In search of bulk-Earth composition. Chemical Geology, 57, 247-267. https://doi.org/10.1016/0009-2541(86)90053-7

836 Hauri, E.H., Saal, A.E., Rutherford, M.J., Van Orman, J.A. (2015). Water in the Moon: Truth
837 and Consequences. Earth and Planetary Science Letters, 409, 252-264.
838 https://doi.org/10.1016/j.epsl.2014.10.053
839
840 Holland, T.J.B., Green, E.C., Powell, R. (2018). Melting of peridotites through to granites: A
841 simple thermodynamic model in the system KNCFMASHTOCr. Journal of Petrology,
842 59, 881-900. https://doi.org/10.1093/petrology/egy048
843
844 Holland, T.J.B., Powell, R. (2011). An improved and extended internally consistent
845 thermodynamic dataset for phases of petrological interest, involving a new equation of
846 state for solids. Journal of Metamorphic Geology, 29, 333-383.
847 https://doi.org/10.1111/j.1525-1314.2010.00923.x
848
849 Hurwitz, D. M., D. A. Kring. (2014). Differentiation of the South Pole–Aitken basin impact
850 melt sheet: Implications for lunar exploration, Journal of Geophysical Research: Planets,
851 119, 1110-1133. https://doi:10.1002/2013JE004530.
852
853 Jennings, E.S., Holland, T.J.B. (2015). A simple thermodynamic model for melting of peridotite
854 in the system NCFMASOCr. Journal of Petrology, 56, 869-892.
855 https://doi.org/10.1093/petrology/egv020
856
857 Jing, J-J., Lin, Y., Knibbe, J.S., van Westrenen, W. (2022). Garnet stability in the deep lunar
858 mantle: Constraints on the physics and chemistry of the interior of the Moon. Earth and
859 Planetary Science Letters, 584, 117491. https://doi.org/10.1016/j.epsl.2022.117491
860
861 Johnson, T.E., Morrissey, L.J., Nemchin, A.A., Gardiner, N.J., Snape, J.F. (2021). The phases of
862 the Moon: Modelling crystallisation of the lunar magma ocean through equilibrium
863 thermodynamics. Earth and Planetary Science Letters, 556, 116721.
864 https://doi.org/10.1016/j.epsl.2020.116721
865
866 Kraettli, G., Schmidt, M.W., Liebske, C. (2002). Garnet stability in the deep lunar mantle:
867 Constraints on the physics and chemistry of the interior of the Moon. EPSL, 584, 117491.
868 https://doi.org/10.1016/j.epsl.2022.117491
869
870 Li, H., Zhang, N., Liang, Y., Wu, B., Dygert, N.J., Huang, J., Parmentier, E.M. (2019). Luna
871 r cumulate mantle overturn: A model constrained by ilmenite rheology. Journal of
872 Geophysical Research: Planets, 124, 1357-1378. https://doi.org/10.1029/2018JE005905
873
874 Lin, Y., Hui, H., Xia, X., Shang, S., van Westrenen, W. (2020). Experimental constraints on the
875 solidification of a hydrous lunar magma ocean. Meteoritics and Planetary Science, 55,
876 207-230. https://doi.org/10.1111/maps.13425
877
878 Lock S.J., Stewart S.T., Cuk, M. (2020). The energy budget and figure of Earth during recovery
879 from the Moon-forming giant impact. Earth and Planetary Science Letters. 530, 115885.
880 https://doi.org/10.1016/j.epsl.2019.115885
881

Lock S.J., Stewart S.T., Petaev, M.I., Leinhardt, Z.M., Mace, M.T., Jacobsen, S. B., Cuk, M. (2018). The origin of the Moon within a terrestrial synestia. Journal of Geophysical Research, 123, 910-951. https://doi.org/10.1002/2017JE005333

Longhi J. (2006). Petrogenesis of picritic mare magmas: Constraints on the extent of early lunar differentiation. Geochimica Cosmochimica Acta, 70, 5919-5934. https://doi.org/10.1016/j.gca.2006.09.023

Maurice, M., Tosi, N., Schwinger, S., Breuer, D., Kleine, T. (2020). A long-lived magma ocean on a young Moon. Science Advances, 6, eaba8949. https://doi.org/10.1126/sciadv.aba8949

McDonough, W.F., Sun, S.-s. (1995). The composition of the Earth. Chemical Geology, 120, 223-253. https://doi.org/10.1016/0009-2541(94)00140-4

Melosh, H.J., Kendall, J., Horgan, B., Johnson, B.C., Bowling, T., Lucey, P.G., Taylor, G.J. (2017). South Pole–Aitken basin ejecta reveal the Moon's upper mantle. Geology, 45, 1063-1066. https://doi.org/10.1130/G39375.1

Palin, R.M., Weller, O.M., Waters, D.J., Dyck, B. (2016). Quantifying geological uncertainty in metamorphic phase equilibria modelling; a Monte Carlo assessment and implications for tectonic interpretations. Geoscience Frontiers, 7, 591-607. https://doi.org/10.1016/j.gsf.2015.08.005

Panning, M.P., Kedar, S., Bowles., N., Bugby, D., Calcutt, S., Elliott, J., et al. (2022). Farside Seismic Suite (FSS): Surviving the lunar night and delivering the first seismic data from the farside of the Moon. Abstract presented at the 53rd Lunar and Planetary Science Conference, Houston, TX.

Papike, J.J., Karner J.M., Shearer, C.K. (2005). Comparative planetary mineralogy: valence state partitioning of Cr, Fe, Ti, and V among crystallographic sites in olivine, pyroxene, and spinel from planetary basalts. American Mineralogist, 90, 277-290. https://doi.org/10.2138/am.2005.1779

Powell, R., Holland, T.J.B. (2008). On thermobarometry. Journal of Metamorphic Geology, 26, 155-179. https://doi.org/10.1111/j.1525-1314.2007.00756.x

Prissel, T.C., Zhang, N., Jackson, C.R.M., Li, H. (2023). Rapid transition from primary to secondary crust building on the Moon explained by mantle overturn. Nature Communications, 14, 11 pp. https://doi.org/10.1038/s41467-023-40751-7

Quillen, A.C., Martini, L., Nakajima, M. (2019). Near/far side asymmetry in the tidally heated Moon. Icarus, 329, 182–196. https://doi.org/10.1016/j.icarus.2019.04.010

Rapp, J.F., Draper, D.S. (2018). Fractional crystallization of the lunar magma ocean: Updating the dominant paradigm. Meteoritics and Planetary Science, 53, 1432-1455. https://doi.org/10.1111/maps.13086

Roy, A., Wright, J.T., Sigurdsson, S. (2014). Earthshine on a young Moon: Explaining the lunar farside highlands. The Astrophysical Journal Letters, 788, L42. https://10.1088/2041-8205/788/2/L42

Sato M., Hickling N.L., McLane, J.E. (1973). Oxygen fugacity values of Apollo 12, 14, and 15 lunar samples and reduced state of lunar magmas. Proceedings of the Lunar Science Conference, 4, 1061-1079.

Schmidt, M.W. Kraettli, G. (2022). Experimental crystallization of the lunar magma ocean, initial selenotherm and density stratification, and implications for crust formation, overturn and the bulk silicate Moon composition. JGR: Planets, 127, e2022JE007187. https://doi.org/10.1029/2022JE007187

Schwinger, S., Breuer, D. (2022). Employing magma ocean crystallization models to constrain structure and composition of the lunar interior. Physics of the Earth and Planetary Interiors, 322, 106831. https://doi.org/10.1016/j.pepi.2021.106831

Sheng, S-Z., Su, B., Wang, S-J., Chen, Y., Li, Q-L., Wang, H., Hui, H., Wu, S., Zhang, B., Yuan, J-Y. (2024). Orthopyroxene-dominated upper mantle melting built the early crust of the Moon. Communications Earth and Environment, 5. https://doi.org/10.1038/s43247-024-01574-6

Snyder, G.A., Taylor, L.A., Neal, C.R. (1992). A chemical model for generating the sources of mare basalts: combined equilibrium and fractional crystallization of the lunar magmasphere. Geochimica et Cosmochimica Acta, 56, 3809-3823. https://doi.org/10.1016/0016-7037(92)90172-F

Solomatov, V.S. (2000). Fluid dynamics of a terrestrial magma ocean. In: Origin of the Earth and Moon, Canup, R.M., Righter, K. (eds.), The University of Arizona Press, Tucson, AZ.

Solomatov, V.S. (2007). Magma oceans and primordial mantle differentiation. In D.J. Stevenson (Ed.), Treatise on Geophysics, Vol. 9: Evolution of the Earth, 91-119.

Spera, F.J. (1992). Lunar magma transport phenomena. Geochimica Cosmochimica Acta, 56, 2253-2265. https://doi.org/10.1016/0016-7037(92)90187-N

Taylor, S.R. (1982). Planetary science: A lunar perspective. Houston, TX: Lunar and Planetary Institute.

Tonks, W.B., Melosh, H.J. (1990). The physics of crystal settling and suspension in a turbulent magma ocean. In H.E. Newsom, J.H. Jones (Eds.), Origin of the Earth, 151-74.

Turcotte, D., Schubert, G. (2002). Geodynamics, 2nd Ed., Cambridge: Cambridge University Press.

Warren, P.H. (1985). The magma ocean concept and lunar evolution. Annual Review of Earth and Planetary Science, 13, 201-240. https://doi:10.1146/annurev.ea.13.050185.001221

Weber, R.C., Lin, P.Y., Garnero, E.J., Williams, Q., Lognonne, P. (2011). Seismic detection of the lunar core. Science, 33, 309-312. https://doi.org/10.1126/science.1199375

White, R.W., Powell, R., Holland, T.J.B., Johnson, T.E., Green, E.C.R. (2014). Progress relating to calculation of partial melting equilibria for metapelites. Journal of Metamorphic Geology, 25, 511-527. https://doi.org/10.1111/j.1525-1314.2007.00711.x

White, R.W., Powell, R., Holland, T J.B., Worley, B. A. (2000). The effect of TiO_2 and Fe_2O_3 on metapelitic assemblages at greenschist and amphibolite facies conditions: mineral equilibria calculations in the system K_2O–FeO–MgO–Al_2O_3–SiO_2–H_2O–TiO_2–Fe_2O_3. Journal of Metamorphic Geology, 18, 497-511. https://doi.org/10.1046/j.1525-1314.2000.00269.x

Wieczorek, M.A., Neumann, G.A., Nimmo, F., Kiefer, W.S., Taylor, G.J., Melosh, H.J,. et al. (2013). The crust of the Moon as seen by GRAIL. Science, 339, 671-675. https://doi.org/10.1126/science.1231530

Williams, J.G., Konopliv, A.S., Boggs, D.H., Park, R.S., Yuan, D-N., Lemoine, F.G., et al. (2014). Lunar interior properties from the GRAIL mission. Journal of Geophysical Research: Planets, 119, 1546-1578. https://doi.org/10.1002/2013JE004559

Wood, M.C., Gréaux, S., Kono, Y., Kakizawa, S., Ishikawa, Y., Inoué, S., et al. (2024). Sound velocities in lunar mantle aggregates at simultaneous high pressures and temperatures: Implications for the presence of garnet in the deep lunar interior. Earth and Planetary Science Letters, 641, 118792. https://doi.org/10.1016/j.epsl.2024.118792

Yamamoto, S., Nagaoka, H., Ohtake, M., Kayama, M., Karouji, Y., Ishihara, Y., Haruyama, J. (2023). Lunar mantle composition based on spectral and geologic analysis of low-Ca pyroxene- and olivine-rich rocks exposed on the lunar surface. Journal of Geophysical Research: Planets, 128, e2023JE007817. https://doi.org/10.1029/2023JE007817

Zhu, M.-H., Wünnemann, K., Potter, R.W.K., Kleine, T., Morbidelli, A. (2019). Are the Moon's nearside-farside asymmetries the result of a giant impact? Journal of Geophysical Research: Planets, 124, 2117-2140. https://doi.org/10.1029/2018JE005826

Zhao, Y., de Vries, J., van den Berg, A.P., Jacobs, M.H.G., van Westrenen, W. (2019). The participation of ilmenite-bearing cumulates in lunar mantle overturn. Earth and Planetary Science Letters, 511, 1-11. https://doi.org/10.1016/j.epsl.2019.01.022

Supporting Information

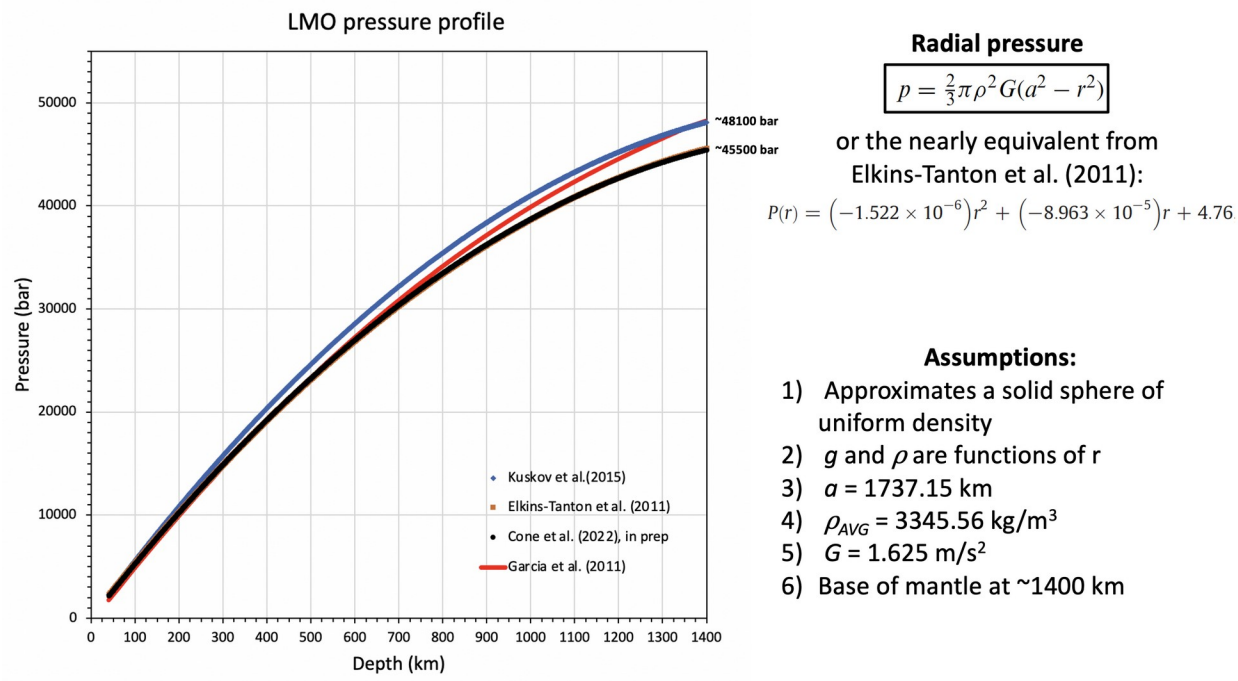

Figure S1. Four pressure-depth profiles from four different works.

Kuskov, O.L., Kronrod, V.A. & Kronrod, E.V. (2015). Thermochemical constraints on the thermal state, composition, and mineralogy of the upper mantle of the Moon: Evidence from the seismic models. Solar System Research, 49, 75–91.

Starting bulk silicate composition (wt.%)

SiO2	46.1000
Al2O3	3.93000
Cr2O3	0.500000
TiO2	0.170000
FeO	7.62000
MgO	38.3000
CaO	3.18000
Na2O	0.050000
K2O	0.003000

Solid solution models in Perple_X

melt(HGP)
Cpx(HGP)
Opx(HGP)
Sp(HGP)
O(HGP)
Gt(HGP)
Pl(JH)
Ilm(WPH)

Grid resolution settings in Perple_X

X_nodes	40 60
Y_nodes	40 60
Initial resolution	1/10 1/24
Grid levels	1 5

Figure S2. Starting values for the LPUM model in Perple_X. See hp633ver.dat for further details. The solid solution model groups HGP, JH, and WPH represent phases defined by Holland, Green and Powell (2018), Jennings and Holland (2015), and White et al. (2000), respectively.

Green et al. (2016) have noted that the solid solution model used here may overpredict ilmenite stability by the inclusion of the geikielite (Ti-Mg bearing) endmember and so "geik" was omitted from our phase equilibria computations.

Holland, T.J.B., Green, E.C., Powell, R. (2018). Melting of peridotites through to granites: A simple thermodynamic model in the system KNCFMASHTOCr. Journal of Petrology, 59, 881-900. https://doi.org/10.1093/petrology/egy048

Jennings, E.S., Holland, T.J.B. (2015). A simple thermodynamic model for melting of peridotite in the system NCFMASOCr. Journal of Petrology, 56, 869-892. https://doi.org/10.1093/petrology/egv020

White, R.W., Powell, R., Holland, T J.B., Worley, B. A. (2000). The effect of TiO_2 and Fe_2O_3 on metapelitic assemblages at greenschist and amphibolite facies conditions: mineral equilibria calculations in the system K_2O–FeO–MgO–Al_2O_3–SiO_2–H_2O–TiO_2–Fe_2O_3. Journal of Metamorphic Geology, 18, 497-511. https://doi.org/10.1046/j.1525-1314.2000.00269.x

Dynamical transition from equilibrium to fractional crystallization

The dynamics of crystal dispersal in a large lunar magma ocean is a complicated problem in geophysical fluid dynamics. Here a scaling analysis is performed to *estimate* the crystal loading (the volume fraction of crystals) at which a thermodynamic regime change from crystal suspension to crystal settling occurs. The physical idea is that the fate of crystals (that is whether they remain substantially suspended except in very thin boundary layers in which some settling will always occur (Martin and Nokes, 1989), or wholesale settle out and accumulate in a basal layer) depends on the magnitude of a dimensionless number R which represents the ratio of crystal settling speed to the rms vertical convective velocity of the LMO. Specifically, three dynamical regimes can be identified. For $R \lesssim 0.1$ crystals will remain suspended due to the action of thermal convection and the magma solidifies by equilibrium crystallization. For $0.1 \lesssim R \lesssim 10$, settling and suspension can both take place depending upon *local* (i.e., spatially variable) values of convection velocities that cannot be predicted by simple scaling. Finally, for $R \gtrsim 10$ crystal settling will predominate, and the magma will solidify by fractional crystallization which precludes earlier formed crystals from reacting with melt. It is important to note that this is a scale analysis and should be viewed in that light. At the same time, the analysis shows how the rheology of magma, specifically the volume fraction of crystals that leads to the viscosity catastrophe, is the dominant effect.

A quantitative scale analysis proceeds by defining a dimensionless parameter:

$$R = \frac{\bigvee_{settling}}{U_{conv}} \tag{1}$$

where the numerator is the crystal settling speed and the denominator the mean rms vertical convective velocity of magma in the LMO. *R*orders and separates the regimes of equilibrium (R small) and fractional crystallization (R large) to first order. Crystal settling velocity is based on a modification of single-particle Stokes settling to allow for hindered settling (Zhu et al., 2019; Pal and Ghoshal, 2013; Cheng, 1997; Chien and Wan, 1983; Garside and Al Diboundi, 1977) for which the 'exponent of reduction' (m) depends on the particle Reynolds number (Re_p). The fundamental expression is constituted by defining terms of R according to

$$\bigvee_{settling} = \bigvee_{Stokes} (1-\theta)^m \tag{2}$$

where $\bigvee_{Stokes}$ is the single particle settling rate in melt

$$\bigvee_{Stokes} = \frac{g \Delta\rho d^2}{18 \eta_{melt}} \tag{3}$$

where g is the acceleration of gravity (1.62 m/s^2), $\Delta\rho$ is the mean crystal- melt density difference, d is the mean crystal diameter and η_{melt} is the dynamic viscosity of melt. The 'exponent of reduction' (m) is a function of the Reynolds number

$$m = \frac{5.1 + 0.27\,\Re_p^{0.9}}{1 + 0.1\,\Re_p^{0.9}} \quad (4)$$

where the particle Reynolds number is defined

$$\Re_p = \frac{\bigvee_{Stokes} \rho_{melt}\, d}{\eta_{melt}} = \frac{\rho_{melt}\, g\, \Delta\rho\, d^3}{18\,\eta_{melt}^2}. \quad (5)$$

Equations (3), (4) and (5) enable estimation of the settling velocity in eq (2) for a crystal of diameter d, in melt of density ρ_{melt} and dynamic viscosity η_{melt} where the density difference between crystal and melt is $\Delta\rho$ and the local volume fraction of crystals is θ. Hence the numerator of eq (1) is determined.

The denominator or eq (1) is evaluated from expressions in Spera (1992) based on the scaling theory of turbulent chaotic high Rayleigh number convection developed by Castaing et al. (1989). The viscous regime scaling for the rms vertical convective velocity (U_{conv}) in the LMO is

$$U_{conv} = \frac{\kappa}{L} Ra^{3/7} ¿¿ \quad (6)$$

where κ is the thermal diffusivity of the LMO, L is the LMO depth, and the thermal Rayleigh number based on melt viscosity is defined

$$Ra = \frac{\rho_{melt} \propto g\, \Delta T\, L^3}{\kappa\, \eta_{melt}}. \quad (7)$$

In eq (7), a is the isobaric expansivity of melt, ΔT is the temperature difference driving convection, and η_{melt} is the viscosity of the LMO melt. The last factor on the RHS of eq (6) accounts for the presence of suspended crystals of volume fraction θ. From Lesher and Spera (2015), the viscosity of Lunar magma depends on the fraction of suspended crystals relative to the viscosity of melt by

$$\eta_{Magma} = \eta_{melt} ¿¿ \quad (8)$$

where C and θ_0 are constants. The former is set equal to three following Lesher and Spera (2015) whereas the latter is a critical packing fraction for viscosity catastrophe. θ_0 depends on the size and shape distribution of crystals (e.g.,Li and Cheng, 1990; Hales, 1992; Jaeger and Nagel, 1992; Daley, 2000; Wyart and Cates, 2014; Vasseur et al, 2021; Wilken et al, 2021). For monodisperse spherical particles, θ_0, the critical packing volume fraction depends on the geometry of packing. For uniform spheres the densest is face-centered cubic packing with a space-filling critical fraction $\theta_0 = \pi/\sqrt{18} \approx 0.74$. The densest random close packing (RCP) for uniform spheres is $\theta_0 \approx$ 0.64 commonly referred to as random close packing (Bernal and Mason, 1960). In random loose packing (RLP) the critical value is about 0.54 (Brouwers, 2014). The critical packing fraction of mixtures of particles with a lognormal distribution, is governed by the standard deviation of sizes, mode of packing, and particle shape and tends to higher values up to or even greater than

$\theta_o \approx 0.8$ (Lam and Nakagawa, 1994). Here we graphically portray R for several values of θ_o to reflect uncertainties regarding crystal characteristics (size and shape distributions) in the LMO.

The final expression for R is found using eqs (2), (3), (4), and (5) together with eqs (6) and (7) to obtain the explicit expression for the ratio of crystal settling speed to rms vertical convective speed

$$R = \frac{\Delta \rho g d^2 L}{18 \kappa \eta_{melt}} Ra^{-3/7} (1-\theta)^m ¿¿ \qquad (9)$$

where the 'exponent of reduction' for crystal settling (m) depends solely on the particle Reynolds number eq (4), C = 3 and θ_0 is the critical packing volume fraction.

Results are shown in the figures below for $\theta_0$equal to θ_0= 0.64 (RCP), θ_0 = 0.74 (face-centered cubic packing) for uniform spheres and θ_0= 0.8 for more variegated mixtures. The value θ_o= 0.64 may be a reasonable compromise. The most important conclusion drawn from analysis of eq (9) is that the regime change from no crystal settling to efficient sedimentation occurs just below the value of critical packing in the neighborhood of θ_0. Although other parameters play a role, the singularity in the two-phase viscosity function at $\theta = \theta_0$ is the dominant effect.

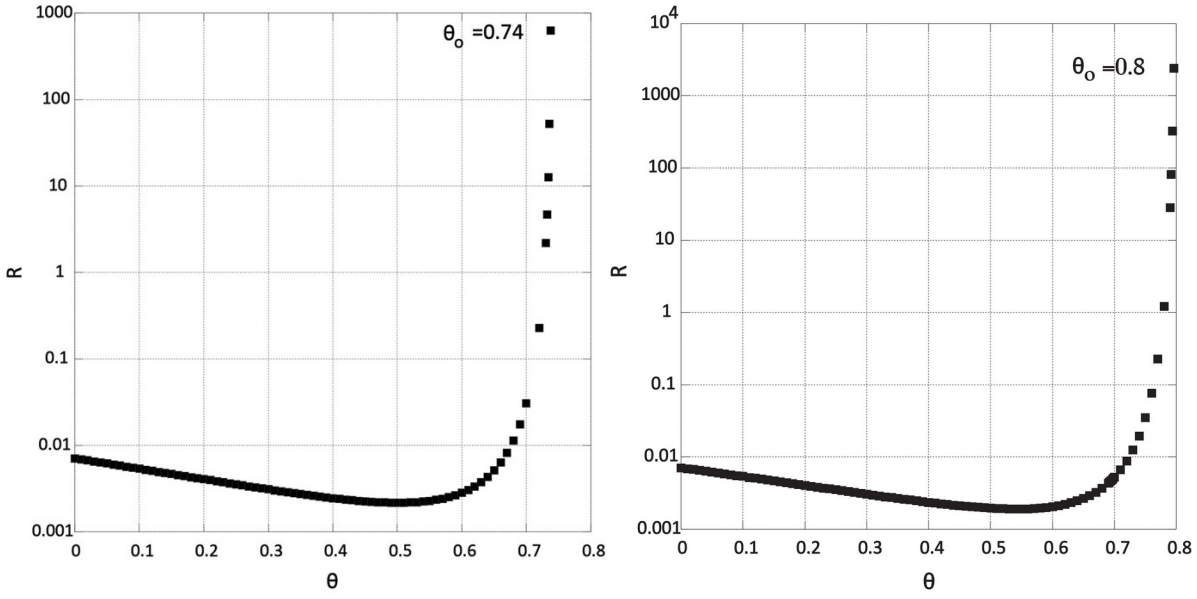

References

Martin, D., & Nokes, R. (1989). A fluid-dynamical study of crystal settling in convecting magmas, Journal of Petrology, 30, 1471–1500. doi:10.1093/petrology/30.6.1471

Zhu, Z., Wang, H., Peng, D., & Dou, J. (2019). Modelling the hindered settling velocity of a falling particle in a particle-fluid mixture by the Tsallis Entropy Theory. Entropy, 21. doi:10.3390/e21010055

Spera, F.J. (1992). Lunar magma transport phenomena. Geochimica et Cosmochimica Acta, 56, 2253–2265. doi:10.1016/0016-7037(92)90187-N

Castaing, B., Gunartatne, G., Heslot, F., Kadanoff, L., Libchaber, A., Thomae, S., ... Zanetti, G. (1989). Scaling of hard thermal turbulence in Rayleigh-Bénard convection. Journal of Fluid Mechanics, 204, 1-30. doi:10.1017/S0022112089001643

Lesher, C.E. & Spera, F.J. (2015). Thermodynamic and Transport Properties of Silicate Melts and Magma. In: Sigurdsson, H., Houghton, B., Rymer, H., Stix, J., McNutt, S. (Eds.), The Encyclopedia of Volcanoes, 113–141.

Richardson, J.F., & Zaki, W.N. (1997). Sedimentation and fluidisation: Part I, Chemical Engineering Research and Design, 75, Supplement, S82-S100. doi:10.1016/S0263-8762(97)80006-8

Garside, J., & Al-Dibouni, M.R. (1977). Velocity-voidage relationships for fluidization and sedimentation in solid-liquid systems. Industrial & Engineering Chemistry Process Design and Development, 16, 206–214. doi:10.1021/i260062a008

Chien, N., & Wan, Z. (1983). Sediment Transport Mechanics, ASCE: Reston, VA.

Cheng, N-S. (1997). Effect of concentration on settling velocity of sediment particles. Journal of Hydraulic Engineering, 123, 728–731.

Pal, D., & Ghoshal, K. (2013). Hindered settling with an apparent particle diameter concept. Advances in Water Resources, 60, 178–187. doi:0.1016/j.advwatres.2013.08.003

Hales, T.C. (1992). The sphere packing problem. Journal of Computational and Applied Mathematics, 44, 41–76. doi:10.1016/0377-0427(92)90052-Y

Li, K., & Cheng, K-H. (1990). On three-dimensional packing. SIAM Journal on Computing, 19, 847 – 867. doi:10.1137/0219059

H. M. Jaeger, H.M., & Nagel, S.R. (1992). Physics of the granular state. Science, 255, 1523–1531. doi:10.1126/science.255.5051.1523

Daley, D.J. (2000). Packing and approximate packing of spheres, Technical Report 104, National Institute of Statistical Sciences.

Wyart, M., & Cates, M.E. (2014). Discontinuous shear thickening without inertia in dense non-Brownian suspensions. Physical Review Letters, 112, 098302. doi: 0.1103/PhysRevLett.112.098302

Bernal, J.D., & Mason, J. (1960). Packing of Spheres: Co-ordination of **r**andomly **p**acked **s**pheres**.** Nature**,** 188, 910–911. doi:10.1038/188910a0

Wilken, S., Guerra, R.E., Levine, D., & Chaikin, P.M. (2021). Random close packing as a dynamical phase transition. Physical Review Letters, 127, 038002. doi:10.1103/PhysRevLett.127.038002}

Brouwers, H.J. (2014). Packing fraction of particles with lognormal size distribution. Physical Review E, 89, 052211. doi: 10.1103/PhysRevE.89.052211

Lam, D.C.C., & Nakagawa, M. (1994). Effect of particle size distribution shape in bimodal packing, Editor(s): N. Mizutani, K. Akashi, T. Kimura, S. Ohno, M. Yoshimura, T. Maruyama, Y. Saito, K. Przybylski, J. Stringer, H. Kawamura, J.-K. Guo, R.O. Ritchie, O. Fukunaga, O. Kamigaito, K. Kijima, J.B. MacChesney, Z.A. Munir, M.I. Boulos, Y. Miyamoto, Z. Nakagawa, M. Mitomo, K. Komeya, R. Metselaar, T.Y. Tien. Advanced Materials '93, 93–96. doi:10.1016/B978-0-444-81991-8.50032-7

Vasseur, J., Wadsworth, F.B., Coumans, J.P., & Dingwell, D.B. (2021). Permeability of packs of polydisperse hard spheres. Physical Review E, 103, 062613. doi:10.1103/PhysRevE.103.062613

FRX60		Bulk oxide wt. %									Cumulate layer phase proportion								Floats porportion								DENSITY (averaged between top and bottom values, NOT BY VOLUME CONTRIBUTION)								
Layer	Layer mid-depth (km)	SiO2	Al2O3	Cr2O3	TiO2	FeO	MgO	CaO	Na2O	K2O	OL	SP	OPX	CPX	ILM	PL	QTZ	SAN	SUM	PL	QTZ	SAN	Bulk solid rho	base melt rho	surf melt rho	OL	SP	OPX	CPX	ILM	PL	QTZ	SAN	mid-depth (km)
22	55.3	71.296	6.309	0.000	0.237	13.166	0.288	6.589	0.501	1.615	0.026			0.248	0.001	0.143	0.488	0.093	1.00				2873.6	NA	NA	4254.4			3576.4	4648.0	2685.6	2551.1	2523.70	55.27
21	56.7	46.287	1.204	0.000	0.575	37.180	1.622	12.537	0.332	0.263	0.073			0.920	0.007				1.00	0.22	0.78	1.0	3641.7	2594.0	2594.0	4222.4			3588.8	4638.5	2700.6	2551.0		56.65
20	59.1	47.267	1.509	0.003	0.645	35.661	2.523	12.028	0.261	0.105				0.992	0.009				1.00	0.23	0.77	1.0	3607.2	2645.0	2632.0				3599.8	4635.5	2704.7	2551.0		59.12
19	62.3	47.099	1.736	0.012	0.894	35.646	4.270	10.172	0.164	0.024				0.987	0.013				1.00	0.57	0.43	1.0	3604.7	2651.0	2653.0				3590.3	4632.7	2707.1	2551.9		62.3382
18	65.9	47.351	2.063	0.032	1.325	32.478	6.964	9.668	0.108	0.010				0.980	0.020				1.00	1.0			3560.1	2726.0	2732.0				3539.5	4627.2	2707.7			65.8946
17	70.5	47.562	2.373	0.067	1.929	28.474	9.417	10.083	0.088	0.006				0.971	0.029				1.00	1.0			3512.1	2786.0	2790.0				3477.7	4621.4	2706.4			70.4669
16	76.3	47.588	2.751	0.122	2.775	23.981	11.920	10.787	0.073	0.004				0.953	0.042				1.00	1.0			3464.7	2833.0	2830.0				3409.8	4615.7	2705.2			76.3402
15	83.7	49.078	3.198	0.181	1.652	20.300	13.659	11.861	0.068	0.004				0.982	0.018				1.00	1.0			3398.1	2858.0	2849.0				3375.4	4613.4	2706.1			83.675
14	91.4	50.632	3.381	0.313	0.811	16.100	16.224	12.481	0.054	0.002			0.043	0.957					1.00	1.0			3328.0	2869.0	2843.0			3347.4	3338.8		2705.5			91.4441
13	99.1	50.302	3.582	0.423	0.680	15.044	17.745	12.174	0.048	0.002	0.039		0.103	0.858					1.00	1.0			3318.1	2872.0	2824.0	3440.4		3328.1	3299.0		2704.1			99.115
12	107.8	50.649	3.948	0.607	0.579	13.160	18.643	12.369	0.043	0.001	0.030		0.176	0.795					1.00	1.0			3298.6	2870.0	2810.0	3367.8		3315.9	3284.0		2703.4			107.833
11	117.9	50.913	4.282	0.860	0.483	12.007	19.845	11.573	0.036	0.001	0.023		0.299	0.678					1.00	1.0			3286.4	2869.0	2795.0	3328.1		3298.9	3263.7		2703.2			117.906
10	130.2	50.506	4.579	1.283	0.331	11.323	23.871	8.082	0.022	0.000	0.077		0.527	0.396					1.00	1.0			3275.1	2864.0	2786.0	3292.1		3284.8	3263.0		2711.0			130.18
9	142.4	50.375	4.129	1.838	0.145	10.545	30.733	2.232	0.003	0.000	0.164	0.001	0.836						1.00				3250.5	2865.0	2790.0	3257.6	4050.5	3245.7						142.44
8	152.8	49.902	3.772	1.850	0.107	9.488	33.205	1.605	0.003	0.000	0.228	0.001	0.771						1.00				3230.6	2873.0	2789.0	3228.8	4066.0	3226.7						152.816
7	163.2	49.046	3.304	1.957	0.079	8.783	35.624	1.203	0.002	0	0.308	0.005	0.687						1.00				3217.2	2882.0	2793.0	3208.3	4073.6	3214.2						163.183
6	174.8	48.347	2.875	1.960	0.059	8.123	37.710	0.925	0.002	0	0.378	0.007	0.615						1.00				3203.6	2893.0	2792.0	3191.5	4084.2	3202.5						174.836
5	187.9	46.956	2.246	1.906	0.039	7.667	40.520	0.663	0.002	0	0.494	0.011	0.496						1.00				3194.1	2904.0	2799.0	3173.7	4090.4	3189.7						187.926
4	201.7	45.546	1.601	1.564	0.024	7.307	43.492	0.465	0.001	0	0.622	0.010	0.368						1.00				3176.1	2915.0	2801.0	3159.4	4099.7	3179.8						201.69
3	208.6	43.873	0.869	0.774	0.013	7.401	46.750	0.318	0.001	0	0.782	0.005	0.214						1.00				3159.3	2927.0	2804.0	3150.8	4092.5	3172.2						208.562
2	231.4	41.822	0.160	0.095	0.002	7.519	50.225	0.176	0.000	0	0.958		0.042						1.00				3143.0	2930.0	2808.0	3143.2		3171.3						231.375
1	249.4	41.413	0.000	0.000	0.000	6.814	51.643	0.130	0.000	0	1.000								1.00				3129.2	2938.0	2813.0	3125.6								249.384

FRX50		Bulk oxide wt. %									Cumulate layer phase proportion								Floats porportion						DENSITY (averaged between top and bottom values, NOT NORMALIZED TO VOLUME CONTRIBUTION)								
Layer	Approx layer mid-depth (km)	SiO2	Al2O3	Cr2O3	TiO2	FeO	MgO	CaO	Na2O	K2O	OL	SP	OPX	CPX	ILM	PL	QTZ	SAN	SUM	PL	QTZ	SAN	Bulk solid rho	base melt rho	surf melt rho	OL	SP	OPX	CPX	ILM	PL	QTZ	SAN	Layer mid-depth (km)
25	60.2	70.586	6.356	0	0.25	13.78	0.32	6.695	0.465	1.55	0.027			0.260	0.002	0.145	0.479	0.088	1.00				2857.6	NA	NA	4252.4			3581.3	4647.3	2690.2	2552.0	2524.40	60.20
24	62.0	47.169	1.440	0.002	0.591	36.287	1.827	12.151	0.311	0.221	0.008			0.984	0.007				1.00	0.24	0.76	1.0	3615.7	2627.2	2610.4				3605.3	4638.3	2703.6	2552.2		62.01
23	65.2	47.110	1.661	0.004	0.717	35.730	2.821	11.662	0.235	0.059				0.990	0.010				1.00	0.26	0.74	1.0	3609.4	2656.3	2643.0				3597.7	4634.6	2706.9	2551.6		65.20
22	68.9	47.831	1.945	0.017	0.246	34.718	5.436	9.670	0.127	0.010				0.984	0.016				1.00	1.00			3594.9	2673.6	2680.2				3578.8	4631.8	2709.2			68.88
21	74.0	47.318	2.295	0.043	1.645	30.831	7.979	9.785	0.097	0.006				0.975	0.025				1.00	1.00			3542.5	2756.4	2770.6				3516.1	4629.9	2708.6			74.03
20	81.3	47.530	2.759	0.094	2.541	25.206	11.243	10.550	0.074	0.004				0.962	0.038				1.00	1.00			3478.2	2831.1	2835.2				3432.8	4618.3	2707.2			81.31
19	89.2	48.717	3.614	0.139	1.620	21.400	13.287	11.147	0.072	0.003				0.984	0.016				1.00	1.00			3419.0	2867.5	2855.1				3396.8	4613.5	2706.2			89.16
18	97.3	50.290	3.751	0.260	0.792	16.945	15.826	12.077	0.057	0.002	0.001		0.040	0.959					1.00	1.00			3342.3	2883.2	2840.2	3496.7		3344.5	3330.1		2705.6			97.32
17	107.4	50.599	3.844	0.430	0.646	14.756	17.569	12.107	0.047	0.001	0.016		0.137	0.847					1.00	1.00			3316.8	2880.9	2829.9	3425.2		3337.2	3301.3		2705.3			107.42
16	118.1	50.837	4.214	0.653	0.526	13.161	18.930	11.640	0.039	0.001	0.016		0.255	0.729					1.00	1.00			3299.8	2879.0	2808.0	3369.2		3317.4	3283.2		2703.9			118.08
15	128.2	51.113	4.571	0.950	0.429	11.818	20.124	10.963	0.032	0.001	0.008		0.375	0.617					1.00	1.00			3286.2	2876.6	2799.8	3324.5		3299.7	3265.3		2704.3			128.15
14	138.9	50.489	5.072	1.453	0.290	11.279	24.038	7.357	0.020	0.000	0.064		0.595	0.341					1.00	1.00			3277.3	2868.6	2793.0	3305.8		3278.2	3260.7		2711.7			138.91
13	150.5	50.253	4.264	1.746	0.164	11.519	29.635	2.415	0.004	0.000	0.152	0.001	0.848						1.00				3264.5	2872.1	2790.0	3270.3	4042.3	3255.6						150.53
12	163.0	49.846	4.015	1.815	0.126	10.581	31.714	1.900	0.003	0.000	0.204	0.002	0.794						1.00				3247.3	2882.6	2795.6	3240.3	4052.9	3235.5						162.96
11	180.6	49.438	3.850	1.739	0.103	9.980	33.101	1.787	0.004	0.000	0.248	0.003	0.749						1.00				3234.3	2890.3	2795.7	3229.0	4059.2	3239.1						180.59
10	187.5	48.992	3.418	1.769	0.080	9.185	35.179	1.374	0.003	0.000	0.306	0.004	0.690						1.00				3219.5	2901.3	2800.6	3200.8	4070.6	3235.4						187.55
9	201.4	48.502	2.829	1.837	0.053	8.116	37.815	0.847	0.002	0.000	0.377	0.006	0.618						1.00				3200.8	2911.1	2800.9	3183.5	4082.2	3200.8						201.36
8	215.2	48.262	2.525	1.784	0.040	7.395	39.323	0.669	0.002	0.000	0.416	0.006	0.578						1.00				3187.5	2920.4	2801.3	3170.0	4087.0	3188.1						215.16
7	229.5	47.160	2.066	1.565	0.030	7.256	41.367	0.554	0.002	0.000	0.510	0.007	0.483						1.00				3178.3	2930.2	2807.6	3163.8	4097.2	3184.8						229.51
6	243.8	46.568	1.650	1.317	0.023	6.830	43.189	0.421	0.002	0.000	0.578	0.006	0.417						1.00				3165.3	2937.7	2808.1	3151.1	4104.7	3184.0						243.82
5	257.9	45.509	1.223	0.911	0.016	6.809	45.190	0.340	0.001	0.000	0.674	0.003	0.322						1.00				3155.2	2946.5	2808.6	3144.5	4095.6	3168.1						257.94
4	272.7	44.263	0.748	0.480	0.009	6.732	47.524	0.242	0.001	0.000	0.785	0.001	0.214						1.00				3143.3	2954.5	2815.5	3138.1	4108.1	3165.6						272.73
3	289	42.570	0.294	0.162	0.004	6.740	50.065	0.166	0.000	0.000	0.915		0.085						1.00				3133.4	2960.2	2817.4	3136.1		3163.4						289.11
2	308	41.550	0.036	0.023	0.000	6.915	51.355	0.120	0.000	0.000	0.989		0.011						1.00				3129.5	2964.7	2820.1	3124.0		3160.6						307.66
1	328	41.561	0.000	0.000	0.000	6.042	52.297	0.099	0.000	0.000	1.000								1.00				3128.5	2972.5	2823.2	3114.0								327.96

FRX50 and FRX60 bulk shell compositions, relative mineral modes, and densities with approximate depths (note to editor: tables/data will be moved to the EarthChem Library for open access after submission).